Draft version November 20, 2023
Typeset using LaTeX **twocolumn** style in AASTeX63

Confinement of the Solar Tachocline by a Non-Axisymmetric Dynamo

Loren I. Matilsky,[1,*] Nicholas H. Brummell,[1] Bradley W. Hindman,[2,3] and Juri Toomre[3]

[1] Department of Applied Mathematics, Baskin School of Engineering University of California, Santa Cruz, CA 96064-1077, USA
[2] Department of Applied Mathematics, University of Colorado Boulder, Boulder, CO 80309-0526, USA
[3] JILA & Department of Astrophysical and Planetary Sciences, University of Colorado Boulder, Boulder, CO 80309-0440, USA

Submitted to ApJ

ABSTRACT

We recently presented the first 3D numerical simulation of the solar interior for which tachocline confinement was achieved by a dynamo-generated magnetic field. In this followup study, we analyze the degree of confinement as the magnetic field strength changes (controlled by varying the magnetic Prandtl number) in a coupled radiative zone (RZ) and convection zone (CZ) system. We broadly find three solution regimes, corresponding to weak, medium, and strong dynamo magnetic field strengths. In the weak-field regime, the large-scale magnetic field is mostly axisymmetric with regular, periodic polarity reversals (reminiscent of the observed solar cycle), but fails to create a confined tachocline. In the strong-field regime, the large-scale field is mostly non-axisymmetric with irregular, quasi-periodic polarity reversals, and creates a confined tachocline. In the medium-field regime, the large-scale field resembles a strong-field dynamo for extended intervals, but intermittently weakens to allow temporary epochs of strong differential rotation. In all regimes, the amplitude of poloidal field strength in the RZ is very well explained by skin-depth arguments, wherein the oscillating field that gives rise to the skin depth (in the medium- and strong-field cases) is a non-axisymmetric field structure rotating with respect to the RZ. These new simulations reaffirm that tachocline confinement by the solar dynamo (the so-called fast magnetic confinement scenario) is possible, but suggest a new picture in which non-axisymmetric field components rotating with respect to the RZ play the primary role, instead of the regularly reversing axisymmetic field associated with the 22-year cycle.

Keywords: Solar dynamo; Solar differential rotation; Solar interior; Solar radiative zone; Solar convective zone

1. THE SOLAR TACHOCLINE

The solar tachocline is a region of primarily radial shear at the base of the solar convection zone (CZ), where strong latitudinal differential rotation transitions to nearly solid-body rotation in the underlying radiative zone (RZ). The tachocline is observed helioseismically to be centered at $r_{t,\odot} \approx 0.69 R_\odot$ (which roughly coincides with the base of the CZ) and to have a thickness of $\Gamma_\odot \lesssim 0.05 R_\odot$ ($\Gamma_\odot$ is too small to be helioseismically resolved, implying that it has an upper bound roughly equal to the helioseismic inversion kernel width; e.g., Howe 2009). Some measurements estimate a wider tachocline ($\Gamma_\odot \lesssim 0.10 R_\odot$; e.g., Kosovichev 1996; Wilson et al. 1996) or a narrower tachocline ($\Gamma_\odot \lesssim 0.02 R_\odot$; e.g., Elliott 1997; Basu & Antia 2003).

Regardless of the true tachocline thickness, even the most liberal estimates for $\Gamma_\odot$ pose a major dynamical problem for solar physics. It is hypothesized (Spiegel & Zahn 1992) that the CZ's differential rotation should spread into the RZ by a process similar to circulation "burrowing" in rotating stably stratified shear flows (e.g., Clark 1973; Haynes et al. 1991), thus widening the tachocline. A shear flow in a rotating system (i.e., differential rotation) is usually accompanied by a horizontal temperature gradient due to thermal wind balance (e.g., Aurnou & Aubert 2011; Matilsky 2023). This gradient tends to spread (burrow) further into the stable layer via

---

Corresponding author: Loren I. Matilsky
loren.matilsky@gmail.com

[*] NSF Astronomy and Astrophysics Postdoctoral Fellow

thermal conduction, carrying with it the circulation and differential rotation associated with the thermal wind. In the Sun, the dominant thermal diffusion is radiative, and Spiegel & Zahn (1992) showed that burrowing (now referred to as "radiative spread") should have increased $\Gamma_\odot$ to $\sim 0.4 R_\odot$ by the current age of the Sun.

Spiegel & Zahn (1992)'s original argument that the solar tachocline should radiatively spread assumes axisymmetry and linearized fluid equations. Under those conditions, radiative spread occurs "hyperdiffusively" (governed by ∇^4 instead of ∇^2) on the solar Eddington-Sweet time $P_{\mathrm{ES},\odot}$. In the hypderdiffusive case, $\Gamma(t)/\Gamma_\odot \sim (t/P_{\mathrm{ES},\odot})^{1/4}$, where $\Gamma(t)$ is the time-dependent tachocline thickness and t is the time since initial confinement (i.e., $\Gamma(0) = \Gamma_\odot$). Since the Eddington-Sweet time is so long for the Sun ($P_{\mathrm{ES},\odot} \approx$ 600 Gyr; see Table B2), this hyperdiffusive property is essential for the burrowing to be significant on time-scales as small as the solar age ($\sim$5 Gyr). Recent 3D fully nonlinear simulations have shown that circulation burrowing does indeed occur in more realistic settings (as long as the time-scales are properly ordered; see Wood & Brummell 2012, 2018). But whether realistic solar burrowing would be hyperdiffusive is still an open question and requires further investigation.

If circulation burrowing is indeed significant for the Sun, it is obvious that there must be a confining (or rigidifying) torque in the RZ to keep $\Gamma_\odot$ under the helioseismically constrained upper bound. There are currently two dominant tachocline confinement scenarios that postulate the origin of this torque. The first, proposed by Spiegel & Zahn (1992), is essentially hydrodynamic. It is supposed that hydrodynamic shear instabilities associated with the differential rotation create turbulence with predominantly horizontal motion, owing to the strong convectively-stable stratification of the RZ. The Reynolds stresses from this horizontal turbulence then act like an enhanced horizontal viscosity, causing preferentially horizontal angular momentum transport, thereby eliminating any burrowing shear on the relatively fast time-scale of months to years. Hence, this scenario is often also called the "fast confinement scenario" (e.g., Gilman 2000; Brun & Browning 2017).

However, similar horizontal turbulence in the Earth's stratosphere is theorized to be "anti-diffusive," that is, transporting angular velocity up the rotation gradient instead of down it and driving the system away from solid-body rotation (e.g., Starr 1968; McIntyre 1994). Angular momentum transport by stratified turbulence in a solar-like system is likely more complicated than simply "diffusive or anti-diffusive." For example, Tobias et al. (2007) argue that horizontal turbulence in the presence of a weak toroidal magnetic field creates Maxwell stresses that nearly exactly cancel the Reynolds stresses, yielding zero net momentum transport. Finally, it remains unclear exactly how anisotropic stratified turbulent transport really is. For example, recent 3D direct numerical simulations (Cope et al. 2020; Garaud 2020) show that meanders of the streamwise flow (in a sufficiently turbulent regime) can vary on small vertical length-scales until secondary vertical shear instabilities (and associated vertical momentum transport) develop.

Gough & McIntyre (1998) proposed an alternative, magnetic confinement scenario. They argued that a weak (minimum $\sim$1 G) poloidal magnetic field in the RZ could resist the shearing motion of any imposed differential rotation via magnetic tension. This magnetic torque would be generated on the time-scale of radiative spread, namely a fraction of $P_{\mathrm{ES},\odot}$. Hence, Gough & McIntyre 1998's scenario is sometimes called the "slow confinement scenario." Note that the fast confinement scenario is mostly hydrodynamic (with magnetism possibly playing a secondary role in modifying the primary baroclinic and shear instabilities), while the slow confinement scenario is fundamentally magnetic.

Finally, a "fast magnetic confinement scenario" has been proposed and modeled in 1D (e.g., Forgács-Dajka & Petrovay 2001; Barnabé et al. 2017), wherein the source of the RZ's poloidal field is the cycling solar dynamo (with the cycle period of $\sim$11 yr, i.e., fast compared to $P_{\mathrm{ES},\odot}$, but slow compared to time-scales associated with most hydrodynamic instabilities) diffusing downward to a skin depth.

We recently presented (Matilsky et al. 2022; hereafter Paper I; see also Matilsky & Toomre 2021), the first 3D numerical simulation of a coupled CZ–RZ system in a spherical shell that spontaneously achieved a magnetically confined tachocline. The source of the magnetism was a non-axisymmetric, quasi-periodic dynamo. In the CZ, the magnetism was topologically similar to the "partial wreaths" (longitudinally-elongated bands of intense toroidal magnetism, with alternating polarity in longitude) identified in our prior CZ-only dynamos (Matilsky & Toomre 2020a,b). We showed in Matilsky & Toomre (2020a) that the partial wreaths in the CZ-only case tended to form a long-lasting magnetic structure that more or less rotates rigidly in a preferred frame. In the combined CZ–RZ tachocline systems considered in the current work, the partial wreaths rotate with respect to the RZ below. As far as the solid-body RZ is concerned, the partial wreaths above resemble a periodically reversing poloidal field and therefore the field diffusively imprints from the overshoot layer to a depth in the RZ consistent with the electromagnetic skin effect.

The main conclusion of the present paper is that the confinement mechanism identified in Paper I can be regarded as a more general version of the fast magnetic confinement scenario that stays robust in a wider parameter space (containing multiple cycling frequency components of the dynamo) and in a 3D geometry with a fully coupled CZ and RZ. Furthermore, a rotating, large-scale *non-axisymmetric* poloidal field structure takes the place of the reversing *axisymmetric* magnetism ("full wreaths") typically invoked in connection with the observed solar cycle, or magnetic butterfly diagram. Our evidence consists of a family of solutions related to the one from Paper I, but with a range of magnetic Prandtl numbers $\mathrm{Pr_m}$. One key effect of varying $\mathrm{Pr_m}$ (while keeping the other control parameters fixed) is to achieve a range of magnetic field strengths in the saturated dynamo state, while keeping other key diagnostic parameters (like the Reynolds and Rossby numbers) relatively unchanged.

The rest of this paper is structured as follows. In Section 2, we describe our equation set and control parameters. In Section 3, we describe the three solution regimes (weak-, medium-, and strong-field) that our dynamos achieve. In Section 4, we present the degree of tachocline confinement, as well as the associated torque balance, for our simulations. In Section 5, we describe the magnetic cycles for the weak- and strong-field cases. In Section 6, we show that for all cases, the poloidal magnetic field strength in the RZ is consistent with diffusive imprinting of the CZ's poloidal according to the electromagnetic skin effect. In Section 7, we highlight the distinctions between axisymmetric and non-axisymmetric polarity reversals. Finally, in Section 8, we discuss our results in the context of the solar tachocline confinement problem.

2. NUMERICAL SCHEME & SIMULATION PARAMETERS

We evolve the 3D magnetohydrodynamic (MHD) equations in spherical shells using the open-source `Rayleigh` code (Featherstone & Hindman 2016; Matsui et al. 2016; Featherstone et al. 2021). We make use of both spherical coordinates—r (radius), θ (colatitude), and ϕ (azimuth angle)—and cylindrical coordinates: $\lambda = r\sin\theta$ (cylindrical radius), ϕ (azimuth angle), and $z = r\cos\theta$ (axial coordinate). The symbol $\hat{\boldsymbol{e}}$ denotes a unit vector. The equations are solved in a frame rotating with the constant angular velocity $\boldsymbol{\Omega}_0 = \Omega_0\hat{\boldsymbol{e}}_z$. The Coriolis force is kept but the oblateness and centrifugal force are ignored. Each shell extends from an inner radius $r_{\rm in}$ to an outer radius $r_{\rm out}$. We divide the shell into two layers of equal depth, separated at $r_0 \equiv (r_{\rm in}+r_{\rm out})/2$. The top half ($r_0$ to $r_{\rm out}$; the CZ) is nominally convectively unstable and the bottom half ($r_{\rm in}$ to r_0; the RZ) convectively stable.

`Rayleigh` solves the anelastic MHD equations, which allow significant density contrast across the shell but disallow sound waves (e.g., Ogura & Phillips 1962; Gough 1969; Gilman & Glatzmaier 1981; Clune et al. 1999). The anelastic approximation consists of assuming a solenoidal mass flux [see Equation (6)] and thermodynamic perturbations that are small relative to a well-chosen "background" or "reference" state. In `Rayleigh`, the background state is always spherically symmetric and time-independent (e.g., Featherstone & Hindman 2016). We choose a background entropy gradient $d\overline{S}/dr$ that changes from stable to unstable near $r = r_0$ over the transition width δ and a gravitational acceleration $\overline{g} = GM_\odot/r^2$ (where $G = 6.67\times10^{-8}$ cm^3 g^{-1} s^{-2} is the universal gravitational constant and $M_\odot = 1.99\times10^{33}$ g the solar mass). If we further assume a hydrostatic, ideal gas (with constant specific heats $c_{\rm v}$ and $c_{\rm p}$), the choices for $d\overline{S}/dr$ and $\overline{g}$ determine the background density $\overline{\rho}$, temperature $\overline{T}$, and squared buoyancy frequency $\overline{N^2} \equiv (\overline{g}/c_{\rm p})d\overline{S}/dr$, which we use in favor of $d\overline{S}/dr$ in the equations.

We choose all diffusivities (kinematic viscosity $\overline{\nu}$, thermal diffusivity $\overline{\kappa}$, and magnetic diffusivity $\overline{\eta}$) to increase with height like $1/\overline{\rho}^{1/2}$. We choose an internal heating function $\overline{Q}$ (representing radiative heating from below) that deposits thermal energy preferentially in roughly the bottom third of the CZ and drives convection. In the RZ, we set $\overline{Q} = 0$, tapered from its profile in the CZ over a width $\delta_{\rm heat}$. We fully describe our reference state in Appendix A and its analogy to the Sun in Appendix B.

The dimensional equations of motion are

$$\nabla\cdot(\overline{\rho}\boldsymbol{u}) = 0, \tag{1}$$

$$\nabla\cdot\boldsymbol{B} = 0, \tag{2}$$

$$\overline{\rho}\left(\frac{D\boldsymbol{u}}{Dt}\right) = -2\overline{\rho}\boldsymbol{\Omega}_0\times\boldsymbol{u} - \overline{\rho}\nabla\left(\frac{P}{\overline{\rho}}\right) + \frac{\overline{\rho}\,\overline{g}S}{c_{\rm p}}\hat{\boldsymbol{e}}_r + \nabla\cdot\boldsymbol{D} + \frac{1}{\mu}(\nabla\times\boldsymbol{B})\times\boldsymbol{B} \tag{3a}$$

$$\text{where}\quad D_{ij} = 2\overline{\rho}\,\overline{\nu}\left[e_{ij} - \frac{1}{3}(\nabla\cdot\boldsymbol{u})\delta_{ij}\right] \tag{3b}$$

$$\text{and}\quad e_{ij} = \frac{1}{2}\left(\frac{\partial u_i}{\partial x_j} + \frac{\partial u_j}{\partial x_i}\right), \tag{3c}$$

$$\overline{\rho}\,\overline{T}\left(\frac{DS}{Dt}\right) = Q - \overline{\rho}\,\overline{T}\frac{d\overline{S}}{dr}u_r + \nabla\cdot\left(\overline{\kappa}\,\overline{\rho}\,\overline{T}\nabla S\right] + D_{ij}e_{ij} + \frac{\eta}{4\pi}|\nabla\times\boldsymbol{B}|^2, \tag{4}$$

and

$$\frac{\partial\boldsymbol{B}}{\partial t} = \nabla\times(\boldsymbol{u}\times\boldsymbol{B} - \eta\nabla\times\boldsymbol{B}). \tag{5}$$

Here, $D/Dt \equiv \partial/\partial t + \boldsymbol{u}\cdot\nabla$ is the material derivative and μ the vacuum permeability ($\mu = 4\pi$ in Gaussian units).

`Rayleigh` was originally run by solving these dimensional equations. In this work, however, we discuss only the equivalent non-dimensional simulations. Length is scaled by the CZ (or RZ) thickness $H \equiv (r_{\rm out} - r_{\rm in})/2$ and time by the rotational time-scale Ω_0^{-1}. The velocity $\boldsymbol{u}$ is scaled by $[\boldsymbol{u}] \equiv \Omega_0 H$ and the vorticity $\boldsymbol{\omega} \equiv \nabla\times\boldsymbol{u}$ by Ω_0 (we use square brackets to denote the unit of each fluid variable). Each background-state profile is scaled by its volume-average over the CZ (denoted by a tilde, e.g., $\tilde{\rho}$), except for $\overline{N^2}$, which is scaled by its volume-average over the RZ (denoted by $\langle\overline{N^2}\rangle_{\rm RZ}$), and $\overline{Q}$, which is scaled as described below. The pressure perturbation P is scaled by $[P] \equiv \tilde{\rho}(\Omega_0 H)^2$ and the magnetic field $\boldsymbol{B}$ by $[\boldsymbol{B}] \equiv \sqrt{\mu\tilde{\rho}}(\Omega_0 H)$.

As noted by Christensen & Aubert (2006), the chosen non-dimensionalization omits the diffusivities from the scales for time and the magnetic field. This is helpful in extending scaling relationships to stellar regimes, where diffusive effects are not believed to play a large role (although we note at the outset that such scaling relationships are likely not present in this work, where diffusive effects *do* play a large role). An added benefit of this non-dimensionalization is that $\boldsymbol{u}$ and $\boldsymbol{B}$ appear with order-unity coefficients in the momentum equation, so their relative importance (to both the force balance and the partition of kinetic and magnetic energy) can be inferred directly from their non-dimensional values.

The internal heating $\overline{Q}$, coupled with the thermal boundary conditions described below, drives convection by establishing sharp entropy gradients in a thermal boundary layer near the top of the CZ (e.g., Featherstone & Hindman 2016; Matilsky et al. 2020). This convection (and conduction, especially in the boundary layer), must carry a "non-radiative" energy flux $\overline{F_{\rm nr}} \equiv (1/r^2)\int_{r_0}^r \overline{Q}(x)x^2dx$ in the statistically steady state. The entropy perturbation S is thus scaled by its estimated difference across the CZ ($[S] = \Delta S \equiv \widetilde{F_{\rm nr}}H/\tilde{\rho}\tilde{T}\tilde{\kappa}$) and $\overline{Q}$ by $\widetilde{F_{\rm nr}}/H$.

With these scaling choices, the non-dimensional equations of motion are

$$\nabla\cdot(\overline{\rho}\boldsymbol{u}) = 0, \tag{6}$$

$$\nabla\cdot\boldsymbol{B} = 0, \tag{7}$$

$$\overline{\rho}\left(\frac{D\boldsymbol{u}}{Dt}\right) = -2\overline{\rho}\hat{\boldsymbol{e}}_z\times\boldsymbol{u} - \overline{\rho}\nabla\left(\frac{P}{\overline{\rho}}\right) + \mathrm{Ra}_{\rm F}^*\overline{\rho}\,\overline{g}S\hat{\boldsymbol{e}}_r + \mathrm{Ek}\nabla\cdot\boldsymbol{D} + (\nabla\times\boldsymbol{B})\times\boldsymbol{B} \tag{8a}$$

$$\text{where}\quad D_{ij} = 2\overline{\rho}\,\overline{\nu}\left[e_{ij} - \frac{1}{3}(\nabla\cdot\boldsymbol{u})\delta_{ij}\right] \tag{8b}$$

$$\text{and}\quad e_{ij} = \frac{1}{2}\left(\frac{\partial u_i}{\partial x_j} + \frac{\partial u_j}{\partial x_i}\right), \tag{8c}$$

$$\overline{\rho}\,\overline{T}\frac{DS}{Dt} = \frac{\mathrm{Ek}}{\mathrm{Pr}}\overline{Q} - \frac{\mathrm{Bu}}{\mathrm{Ra}_{\rm F}^*}\overline{\rho}\,\overline{T}\frac{\overline{N^2}}{\overline{g}}u_r + \frac{\mathrm{Ek}}{\mathrm{Pr}}\nabla\cdot(\overline{\rho}\,\overline{T}\,\overline{\kappa}\nabla S) + \frac{\mathrm{DiEk}}{\mathrm{Ra}_{\rm F}^*}D_{ij}e_{ij} + \frac{\mathrm{DiEk}}{\mathrm{Pr_m Ra}_{\rm F}^*}\overline{\eta}|\nabla\times\boldsymbol{B}|^2, \tag{9}$$

$$\text{and}\quad \frac{\partial\boldsymbol{B}}{\partial t} = \nabla\times(\boldsymbol{u}\times\boldsymbol{B}) - \frac{\mathrm{Ek}}{\mathrm{Pr_m}}\nabla\times(\overline{\eta}\nabla\times\boldsymbol{B}). \tag{10}$$

All field variables ($\boldsymbol{u}$, $\boldsymbol{B}$, S, and P), spatial quantities (r, t, λ, z, and ∇), and background-state profiles now denote their non-dimensional values. The non-dimensional input numbers (definitions and values) are given in Table 1.

The reference-state control parameters are the ratio of specific heats γ, the CZ-to-RZ aspect ratio α, the CZ aspect ratio β, the number of scale heights across the CZ N_ρ, and the transition widths δ and $\delta_{\rm heat}$. This reference state (except for the diffusivity profiles) is reasonably solar-like and describes the upper 2.1 density scale-heights of the solar RZ and the lower 3 density scale-heights of the solar CZ (see Appendix A). In units of H, the non-dimensional solar radius is $R_\odot = 4.39$ (we plot radial profiles as functions of $r/R_\odot$, to more easily compare to prior work).

The fluid control parameters are the Prandtl number Pr, the magnetic Prandtl number $\mathrm{Pr_m}$, the modified Rayleigh number $\mathrm{Ra}_{\rm F}^*$, the Ekman number Ek, and the buoyancy number Bu. The dissipation number $\mathrm{Di} \equiv \tilde{g}H/(c_{\rm p}\tilde{T}) = 1.72$ for the cases here and is not a control parameter in our convention, being a function of γ, β, and N_ρ, which we deem reference state control parameters (see Appendix A and Korre & Featherstone 2021). Some additional parameters (that can be derived from the input parameters given in Table 1) are given in Table A1.

Equations (6)–(10) are discretized in space. For all simulations, we use three sets of stacked Chebyshev collocation points in r ($N_r/3 = 64$ points in each domain), $N_\theta = 384$ Legendre collocation points in θ, and $N_\phi = 2N_\theta = 768$ uniformly spaced collocation points

Table 1. Non-dimensional control parameters for our simulations. We list reference-state parameters first, then the fluid control parameters.

Parameter	Definition	Value
γ	$c_{\rm p}/c_{\rm v}$	5/3
α	$(r_{\rm out}-r_0)/(r_0-r_{\rm in})$	1
β	$r_0/r_{\rm out}$	0.759
N_ρ	$\ln[\overline{\rho}(r_0)/\overline{\rho}(r_{\rm out})]$	3.00
δ	stability transition width	0.219
$\delta_{\rm heat}$	heating transition width	0.132
Pr	$\tilde{\nu}/\tilde{\kappa}$	1
$\rm Pr_m$	$\tilde{\nu}/\tilde{\eta}$	1 to 8
$\rm Ra_F^*$	$\widetilde{F_{\rm nr}}\tilde{g}/(c_{\rm p}\tilde{\rho}\tilde{T}\tilde{\kappa}\Omega^2)$	0.638
Ek	$\tilde{\nu}/(\Omega_0 H^2)$	1.07×10^{-3}
Bu	$\langle N^2\rangle_{\rm RZ}/\Omega_0^2$	2.54×10^{4}

in ϕ. The Chebyshev points cluster near each domain's boundaries. We require increased resolution in the overshoot layer (i.e., in the vicinity of $r_0/R_\odot=0.719$), and so we set the radial domain boundaries at $r/R_\odot=\{0.491,0.669,0.719,0.947\}$ (or equivalently, $r-r_0=\{-1.000,-0.219,0.000,1.000\}$). Nonlinear terms and the Coriolis force are evaluated in physical space (i.e., on the discretized spatial grid), while the remaining linear terms are evaluated in spectral space, using Chebyshev polynomials in each r sub-domain and spherical harmonics in θ and ϕ. The variables in physical space are de-aliased using the 2/3 rule: the maximum Chebyshev degree (in each r sub-domain) is $n_{\rm max}=42$ and the maximum spherical harmonic degree is $\ell_{\rm max}=255$. For more details, see Glatzmaier (1984) and Clune et al. (1999), who pioneered `Rayleigh`'s pseudo-spectral algorithm.

Each magnetic simulation differs only in the choice of $\rm Pr_m$, which ranges from 1 to 8. We also consider a purely hydrodynamic simulation (referred to as "case H"), which has all the parameters listed in Table 1, but no magnetic field. We refer to each magnetic case by its value of $\rm Pr_m$ rounded to two decimal places: e.g., "case 1.08" means $\rm Pr_m=1.076$. Cases H and 4.00 were analyzed in Paper I. All chosen values of $\rm Pr_m$ are listed in Table 2.

At both boundaries, we use stress-free and impenetrable conditions on $\boldsymbol{u}$, potential-field-matching conditions on $\boldsymbol{B}$, and fixed-entropy-gradient conditions on S. Specifically, we set $\partial S/\partial r$ to zero at the bottom boundary (thus allowing no conductive flux in or out) and set it to a latitudinally-independent negative value at the top boundary, such that the energy conducted out the top is equal to the energy injected by $\overline{Q}$ (e.g., Matilsky et al. 2020). The convection is initialized by introducing weak noise in S (amplitude $\sim10^{-3}$), randomly distributed in space throughout the entire shell. For the magnetic cases, we further introduce weak noise in $\boldsymbol{B}$ (amplitude $\sim10^{-6}$), randomly distributed in space throughout the CZ only. The other field variables ($\boldsymbol{u}$ and P) are initialized to zero in all space.

We use several types of averages in this work. Let $\psi=\psi(r,\theta,\phi,t)$ denote a scalar quantity (or a single component of a vector quantity) dependent on position and time. Then $\langle\psi\rangle_\phi$, $\langle\psi\rangle_{\rm sph}$, $\langle\psi\rangle_{\rm CZ}$, $\langle\psi\rangle_{\rm RZ}$, and $\langle\psi\rangle_{\rm full}$ denote instantaneous averages of ψ over longitude, spherical surfaces, the CZ (volume-average from r_0 to $r_{\rm out}$), the RZ (volume-average from $r_{\rm in}$ to r_0), and the full shell (volume-average from $r_{\rm in}$ to $r_{\rm out}$), respectively. An additional temporal average (over the "equilibrated state"; see the following section) is denoted by appending a "t" to the subscript in the average: e.g., $\langle\psi\rangle_{\phi,t}$. Subtracting the instantaneous longitudinal average is denoted by a prime: $\psi'\equiv\psi-\langle\psi\rangle_\phi$. We also colloquially refer to $\langle\psi\rangle_\phi$ and ψ' as the "mean and fluctuating" components of ψ, respectively.

3. DYNAMO REGIMES

All the magnetic cases presented here yield sustained large-scale dynamos. As convection and dynamo action become significant, the field variables grow from their initially small values to amplitudes of order unity. We quantify this growth in terms of the kinetic energy density of the differential rotation, $\rm KE_{DR}$, and the magnetic energy density, ME:

$$\mathrm{KE_{DR}}\equiv\frac{1}{2}\overline{\rho}\,\langle u_\phi\rangle_\phi^2\qquad\text{and}\qquad\mathrm{ME}\equiv\frac{1}{2}\left\langle\boldsymbol{B}^2\right\rangle_\phi.\tag{11}$$

In Figure 1, we show the growth and long-term behavior of the volume-averaged energy densities for some representative simulations. After a certain time (which we call $t=t_{\rm eq}$), the system achieves a "statistically steady" or "equilibrated" state, in which the volume-averaged magnitude of each field variable fluctuates about a well-defined temporal mean. We choose $t_{\rm eq}$ (fairly roughly) by eye from plots like Figure 1(a). For example, we choose $t_{\rm eq}=2000P_{\rm rot}$ for case 1.06, $t_{\rm eq}=1000P_{\rm rot}$ for case 2.00, and $t_{\rm eq}=600P_{\rm rot}$ for case 4.00 (see Table 2 for all values of $t_{\rm eq}$).

Figure 1(a) suggests three basic dynamo regimes. The low-$\rm Pr_m$ solution (case 1.06; blue curves) lies in a "weak-field regime", characterized by ME orders of magnitude weaker than $\rm KE_{DR}$. There is a regular magnetic energy cycle, with a period of roughly 750 $P_{\rm rot}$. The high-$\rm Pr_m$ solution (case 4.00; red curves) lies in a "strong-field regime", characterized by ME about in equipartition with $\rm KE_{DR}$ and $\rm KE_{DR}$ itself much weaker than in

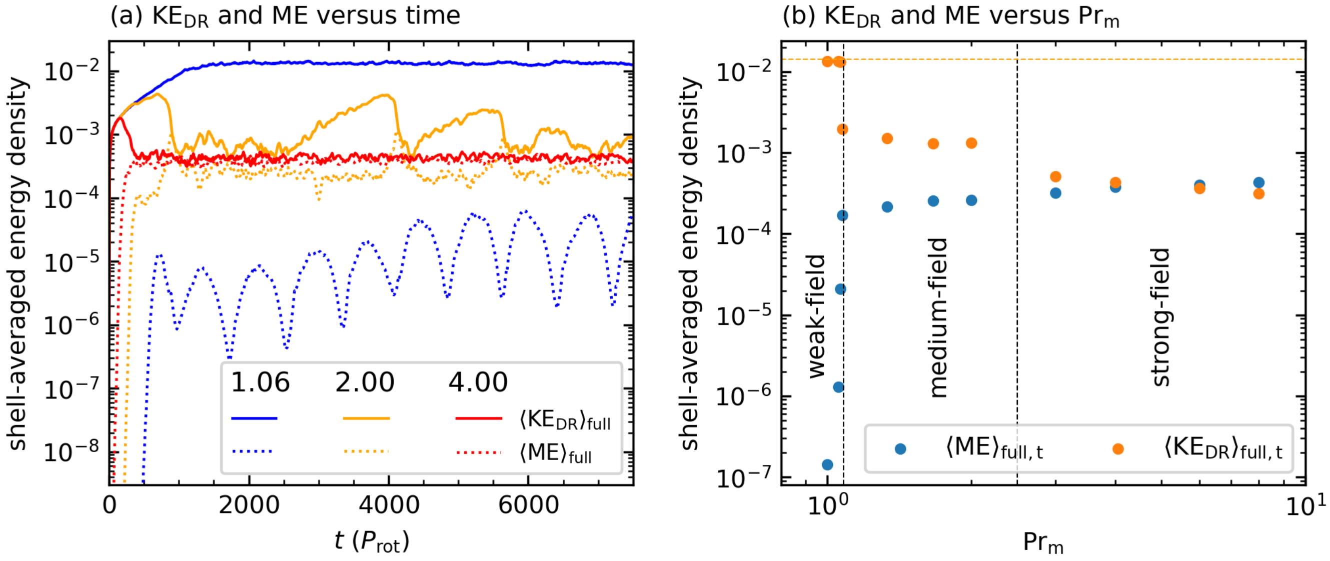

Figure 1. Averaged KE and ME as functions of time and $\mathrm{Pr_m}$. (a) $\langle\mathrm{KE}\rangle_{\mathrm{full}}$ (solid curves) and $\langle\mathrm{ME}\rangle_{\mathrm{full}}$ (dashed curves) with respect to time for three values of $\mathrm{Pr_m}$ (indicated by three different line colors and legend headings). (b) $\langle\mathrm{KE}\rangle_{\mathrm{full,t}}$ and $\langle\mathrm{ME}\rangle_{\mathrm{full,t}}$ for all magnetic simulations. Vertical black lines denote tentative regime boundaries and the horizontal orange line marks $\langle\mathrm{KE}\rangle_{\mathrm{full,t}}$ for case H.

the weak-field case. Finally, the intermediate-$\mathrm{Pr_m}$ solution (case 2.00; orange curves) lies in a "medium-field regime." Case 2.00 has properties similar to those of a strong-field dynamo some of the time, but occasionally ME falls below its strong-field value and then $\mathrm{KE_{DR}}$ steadily increases above its strong-field value (representing an increase in differential rotation or partial disappearance of the tachocline). After $\mathrm{KE_{DR}}$ reaches a critical level, ME grows rapidly, lowering $\mathrm{KE_{DR}}$ back to its lower, strong-field value. There is no clear cycling behavior, obvious physical trigger, or general predictability for the medium-field cases' temporary epochs of strong differential rotation.

Figure 1(b) shows the equilibrated levels of the kinetic energy in the differential rotation, $\langle\mathrm{KE_{DR}}\rangle_{\mathrm{full},t}$, and the magnetic energy, $\langle\mathrm{ME}\rangle_{\mathrm{full},t}$, for all simulations. The "weak-field" regime (for which the differential rotation has the same magnitude as in case H) sits in the narrow range of roughly $1.00 \lesssim \mathrm{Pr_m} \lesssim 1.06$. The "medium-field" regime (for which the differential rotation is substantially weakened compared to the weak-field cases but intermittently becomes stronger) occupies roughly $1.08 \lesssim \mathrm{Pr_m} \lesssim 2.5$. The "strong-field" regime (lowest differential rotation and highest magnetic energy) occupies $\mathrm{Pr_m} \gtrsim 2.5$. Note that these identified regimes and their boundaries are only suggestive, given our limited resolution in $\mathrm{Pr_m}$-space.

The weak-field dynamos tend to be more axisymmetric (magnetism dominated by azimuthal wavenumber $m = 0$) than the strong-field dynamos. Figure 2 shows the toroidal magnetic field projected on spherical surfaces for four solutions at different $\mathrm{Pr_m}$ and therefore in the different regimes. For case 1.00 (the weak-field regime), there is a strong $m = 0$ component, both in the CZ and even more so in the RZ. For higher values of $\mathrm{Pr_m}$ (the medium- and strong-field regimes), the field in the CZ becomes increasingly dominated by small scales, but retains a large-scale ($m = 1, 2$) envelope. For the all cases, the RZ appears to act as a low-pass filter for the spatial scales of the field, letting only the low m's survive. This is especially apparent for case 8.00 (Figures 2(g,h)).

As a whole, the $m = 0$ structures at low $\mathrm{Pr_m}$ resemble what has previously been called magnetic "wreaths"—toroidal bands of strong magnetism looping the full sphere in a given hemisphere (e.g., Brown et al. 2010; Passos & Charbonneau 2014; Bice & Toomre 2020). Such wreaths are often invoked in connection to the magnetic butterfly diagram, as interior reservoirs of toroidal field from which smaller loops can potentially break off and buoyantly rise to form sunspot pairs (e.g., D'Silva & Choudhuri 1993; Stenflo & Kosovichev 2012; Nelson et al. 2013a; Li 2018; Bice & Toomre 2023).

For higher $\mathrm{Pr_m}$, the strong $m = 1, 2$ components of $\boldsymbol{B}$ resemble the "partial wreaths" discussed at some length by Matilsky & Toomre (2020a). The cases from that paper contained a dominant $m = 1$ field structure that appeared to be two opposite-polarity full wreaths tilted into each other, or possibly linked. On a spherical slice, the tilted full wreaths showed up as two opposite-

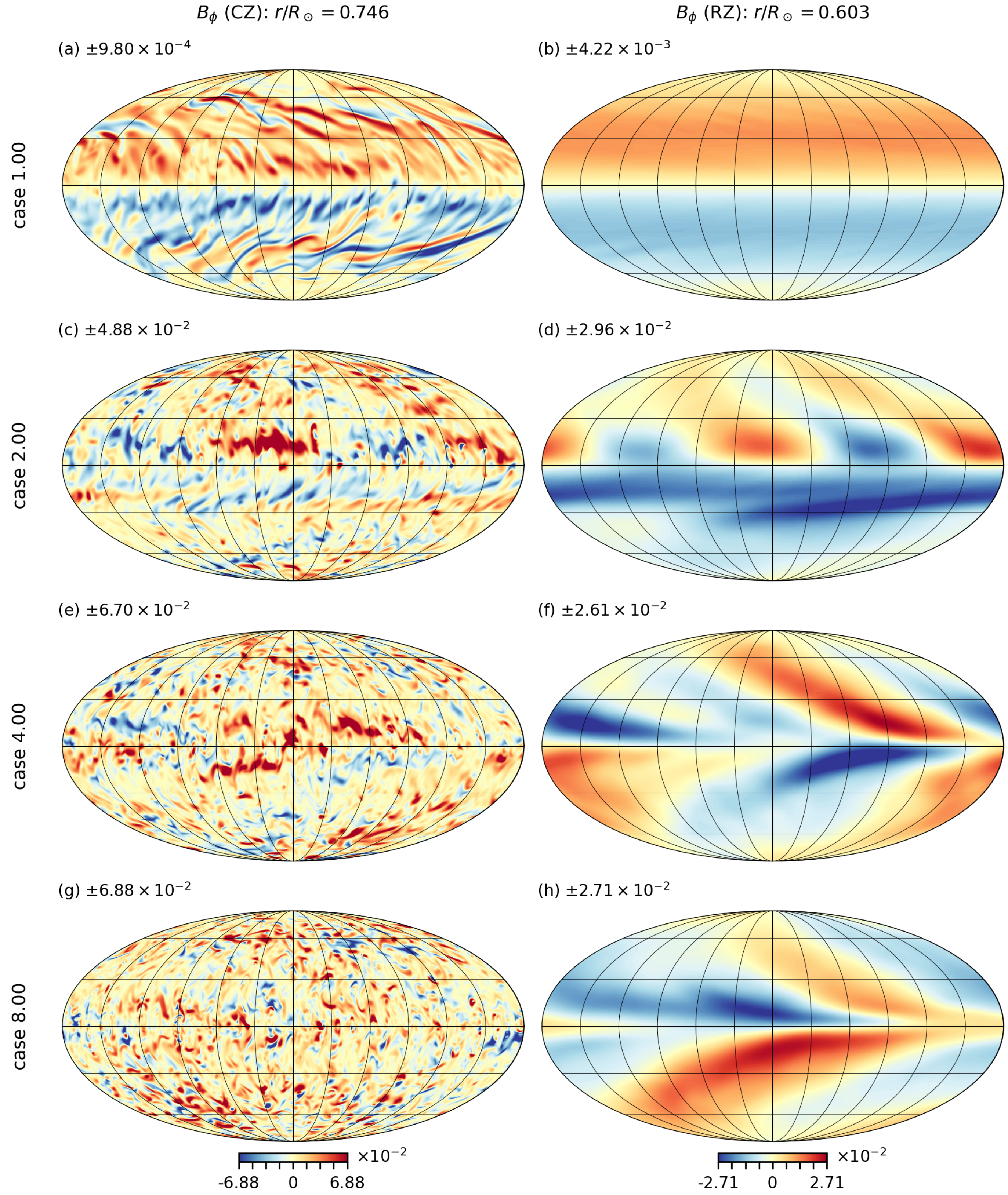

Figure 2. Mollweide projections of the toroidal magnetic field B_ϕ on spherical surfaces for four chosen values of $\mathrm{Pr_m}$ at time $t = 3500 P_{\mathrm{rot}}$. Each $\mathrm{Pr_m}$ corresponds to a different row (pair) of Mollweides, and $\mathrm{Pr_m}$ increases downward. The spherical surfaces are at two radii, one near the base of the CZ (left-hand column) and one in the middle of the RZ (right-hand column). The colorbar (shown for the bottom row only) is the same for all figures and we give its saturation values next to the alphabetical labels.

polarity "partial wreaths", extending in longitude by about 180°, with central longitudes on opposite sides of the sphere. We should note that "partial wreath" is really a placeholder for lack of a better term. The 3D field-line tracings of these non-axisymmetric structures tend to be quite difficult to interpret and it remains unclear exactly what topology (linked wreaths, tilted wreaths, or even open field-lines) is leading to the two-dimensional projections shown in Figure 2.

To quantify the non-axisymmetry in our dynamos more precisely, we partition the magnetic energy according to m-value. We define the m-component of $\boldsymbol{B}$ through

$$\boldsymbol{B}_m \equiv \left\langle \boldsymbol{B} e^{-im\phi} \right\rangle_\phi \tag{12a}$$

$$\text{or} \qquad \boldsymbol{B} \equiv \sum_m \boldsymbol{B}_m e^{im\phi}. \tag{12b}$$

Note that since $\langle \cdots \rangle_\phi$ is computed by averaging over the uniformly spaced ϕ-grid, Equation (12) represents the forward and inverse discrete Fourier transforms (DFTs) in ϕ. For the chosen normalization, Parceval's theorem takes the form

$$\left\langle \boldsymbol{B}^2 \right\rangle_\phi = \sum_m |\boldsymbol{B}_m|^2. \tag{13}$$

Note that by definition, $\boldsymbol{B}_0 = \langle \boldsymbol{B} \rangle_\phi$. Different components of the magnetic energy are thus attributed to different m-components of $\boldsymbol{B}$.

Table 2 shows some basic simulation properties ($\mathrm{Pr_m}$, regime, total run time $t_{\max}$, and equilibration time t_{eq}), as well as the partitions of kinetic and magnetic energy for each simulation.[1] We define the magnetic field strength of the "small-scale field" by $\mathrm{ME}_{\geq 3} \equiv (1/2)\sum_{|m|\geq 3} |\boldsymbol{B}_m|^2$. With increasing $\mathrm{Pr_m}$, the fraction of magnetic energy in the small-scale fields ($\mathrm{ME}_{\geq 3}/\mathrm{ME}$) increases, as might be expected from the more prominent small-scale structures seen in Figure 2 at higher $\mathrm{Pr_m}$. The deficit, i.e., the fraction of energy in the large-scale fields ($m = 0, 1, 2$) decreases, but the partition between each m-component is complex.

For the weak-field cases, in both the CZ and RZ, the power in the axisymmetric field dominates over that in the $m = 1, 2$ components. But for the medium- and strong-field cases, there seems to be no general rule for whether $m = 0, 1,$ or 2 dominates. One robust feature is that in all regimes, the magnetic energy in the RZ is stored primarily in the large-scale fields. Even for the strongest-field case 8.00, the small-scale ($|m| \geq 3$) field components account for only ~30% of the magnetic energy. These results strengthen the earlier idea that the RZ acts as a low-pass filter, letting in only the lowest-m components of the field. Such behavior is expected if the field evolution in the RZ is primarily governed by diffusion, an idea we return to in Section 6, where we discuss the skin-effect behavior of the poloidal field.

4. TACHOCLINE CONFINEMENT

4.1. *Tachocline Appearance*

All dynamos in the medium- and strong-field regimes sustain tachoclines. To describe them, we define the rotation rate Ω (as measured in the rotating frame):

$$\Omega(r,\theta) \equiv \frac{\langle u_\phi \rangle_{\phi,t}}{\lambda}. \tag{14}$$

Figure 3 shows Ω for a weak-, medium-, and strong-field case, as well as the Sun. The weak-field case does not have a tachocline and has rotation rate nearly identical to that of case H, that is, there is strong latitudinal rotation contrast in the CZ ($\Delta\Omega_{\mathrm{CZ}} \sim 0.2$, similar to the solar value), which imprints throughout the entire RZ (for case H's rotation profile, see Paper I).

By contrast, the medium- and strong-field cases all have tachoclines, that is, there is (weak) differential rotation in the CZ, but nearly solid-body rotation in the RZ. The radial transition from differential to solid-body rotation appears quite abrupt at most latitudes from the color plots in Figures 3(b,c), suggesting thin simulated tachoclines. However, this visual abruptness is partly due to our choice of bi-linear colormap for the asymmetric values of Ω about 0. This colormap deepens the blue tones in the CZ at high latitudes. As we now demonstrate, the simulated tachoclines (after they are fit systematically) are in fact about twice as thick as the solar one.

We define the radially varying latitudinal differential rotation contrast $\Delta\Omega(r)$:

$$\Delta\Omega(r) \equiv \Omega(r,\pi/2) - \frac{1}{2}[\Omega(r,\pi/6) + \Omega(r,5\pi/6)], \tag{15}$$

i.e., the difference in rotation rate between the equator and the average rate of 60° latitude north and south. We define the rotation contrasts in the CZ and RZ, and their ratio:

$$\Delta\Omega_{\mathrm{CZ}} \equiv \langle \Delta\Omega \rangle_{\mathrm{CZ}}, \tag{16a}$$

$$\Delta\Omega_{\mathrm{RZ}} \equiv \langle \Delta\Omega \rangle_{\mathrm{RZ}}, \tag{16b}$$

$$\text{and} \qquad f \equiv \frac{\Delta\Omega_{\mathrm{RZ}}}{\Delta\Omega_{\mathrm{CZ}}}, \tag{16c}$$

---

[1] For completeness and reproducibility, we also give the Reynolds, Rossby, and magnetic Reynolds numbers for each case in Appendix C.

Table 2. Basic simulation properties ($\mathrm{Pr_m}$, regime, run time t_{max}, and equilibration time t_{eq}) and partition of kinetic and magnetic energy for each simulation's CZ and RZ. Here we define the kinetic energy of the convection (fluctuating flows) as $\mathrm{KE_c} \equiv (1/2)\overline{\rho}\left\langle(\boldsymbol{u}')^2\right\rangle_\phi$. The diffusion time P_{diff} refers to the viscous (or equivalently, thermal) diffusion time $P_\nu = P_\kappa$ for case H and to the magnetic diffusion time P_η for the magnetic cases (see Table A1). The letters "W," "M," and "S," denote the weak-, medium-, and strong-field regimes, respectively. For the energy ratios, a volumetric (over the CZ or RZ) and temporal mean is implied for the numerator and denominator separately. For example, "$2|\boldsymbol{B}_1|^2/\boldsymbol{B}^2$" in the "CZ" section should be read as $2\left\langle|\boldsymbol{B}_1|^2\right\rangle_{\mathrm{CZ},t} / \left\langle\boldsymbol{B}^2\right\rangle_{\mathrm{CZ},t}$. The factors of 2 account for the symmetry $|\boldsymbol{B}_{-m}|^2 = |\boldsymbol{B}_m|^2$ (since $\boldsymbol{B}$ is real).

Case	H	1.00	1.05	1.06	1.08	1.33	1.67	2.00	3.00	4.00	6.00	8.00
$\mathrm{Pr_m}$	-	1.000	1.054	1.065	1.076	1.333	1.667	2.000	3.000	4.000	6.000	8.000
regime	-	W	W	W	M	M	M	M	S	S	S	S
$t_{\mathrm{eq}}/P_{\mathrm{rot}}$	1000	1500	1500	2000	2300	1500	1200	1000	1700	600	500	500
$t_{\mathrm{max}}/P_{\mathrm{rot}}$	9930	9740	6670	7770	9400	7480	8170	9200	7730	16000	5450	5750
$t_{\mathrm{max}}/P_{\mathrm{diff}}$	12.7	12.5	8.13	9.36	11.2	7.20	6.29	5.90	3.31	5.15	1.17	0.92
CZ energy density parameters												
$\mathrm{KE_{DR}}$	0.011	0.011	0.011	0.011	2.05e-3	1.83e-3	1.24e-3	1.25e-3	4.70e-4	3.75e-4	2.82e-4	2.19e-4
$\mathrm{KE_c}$	1.71e-3	1.71e-3	1.69e-3	1.69e-3	9.71e-4	9.52e-4	9.35e-4	9.31e-4	9.08e-4	8.90e-4	8.74e-4	8.58e-4
ME	-	1.99e-8	1.82e-7	3.16e-6	1.56e-4	2.08e-4	2.72e-4	2.94e-4	4.21e-4	5.08e-4	5.52e-4	5.98e-4
$\langle\boldsymbol{B}\rangle_\phi^2/\boldsymbol{B}^2$	-	0.389	0.371	0.334	0.088	0.108	0.077	0.066	0.028	0.021	0.017	0.013
$2\lvert\boldsymbol{B}_1\rvert^2/\boldsymbol{B}^2$	-	0.042	0.042	0.043	0.248	0.156	0.144	0.117	0.121	0.106	0.064	0.044
$2\lvert\boldsymbol{B}_2\rvert^2/\boldsymbol{B}^2$	-	0.040	0.042	0.067	0.165	0.179	0.162	0.149	0.091	0.063	0.046	0.041
$\mathrm{ME}_{\geq 3}/\mathrm{ME}$	-	0.529	0.545	0.556	0.499	0.556	0.617	0.668	0.760	0.809	0.874	0.902
RZ energy density parameters												
$\mathrm{KE_{DR}}$	0.016	0.016	0.016	0.016	1.20e-3	1.30e-3	8.97e-4	9.40e-4	5.33e-5	3.62e-5	3.17e-5	2.38e-5
$\mathrm{KE_c}$	4.14e-4	4.14e-4	4.00e-4	4.09e-4	5.37e-5	4.03e-5	3.12e-5	2.98e-5	2.28e-5	2.18e-5	2.03e-5	1.90e-5
ME	-	3.71e-7	3.41e-6	5.47e-5	1.97e-4	2.26e-4	2.28e-4	2.09e-4	1.36e-4	1.38e-4	1.34e-4	1.28e-4
$\langle\boldsymbol{B}\rangle_\phi^2/\boldsymbol{B}^2$	-	0.957	0.955	0.957	0.527	0.658	0.603	0.587	0.117	0.076	0.127	0.096
$2\lvert\boldsymbol{B}_1\rvert^2/\boldsymbol{B}^2$	-	5.01e-3	5.02e-3	5.10e-3	0.320	0.151	0.161	0.149	0.399	0.446	0.397	0.359
$2\lvert\boldsymbol{B}_2\rvert^2/\boldsymbol{B}^2$	-	4.21e-3	4.33e-3	4.53e-3	0.098	0.132	0.162	0.172	0.273	0.242	0.210	0.249
$\mathrm{ME}_{\geq 3}/\mathrm{ME}$	-	0.034	0.035	0.033	0.054	0.059	0.074	0.092	0.210	0.236	0.266	0.296

respectively. Because the medium- and strong-field RZs often rotate like solid bodies, we define the (volume-averaged) constant rotation rate of the RZ:

$$\Omega_{\mathrm{RZ}} \equiv \langle\Omega\rangle_{\mathrm{RZ}} \tag{17}$$

Figure 4 shows line plots of the rotation rate along radial lines for the Sun and case 4.00. Clearly in the solar case, the tachocline is confined to a relatively narrow radial layer, with strong differential rotation in most of the CZ and very little in the RZ, indicating a large $\Delta\Omega_{\mathrm{CZ}}$, a small $\Delta\Omega_{\mathrm{RZ}}$, and therefore small f for the true solar case. By contrast, in case 4.00, while $\Delta\Omega_{\mathrm{RZ}}$ is severely diminished, thus indicating that the RZ rotates nearly as a solid body, $\Delta\Omega_{\mathrm{CZ}}$ is also significantly diminished.

A further deviation from the solar case is that our simulated rotation profiles have most of the differential rotation contrast confined to a low-latitude band between about ±30°. The result is relatively strong radial shear distributed far more evenly throughout the CZ in the simulations than in the Sun. Equivalently, each simulated tachocline is not thin, but basically occupies the whole convective layer and is centered near mid-CZ, well above r_0.

In order to define the location and width of the simulated tachoclines, we define:

$$\psi(r) \equiv \frac{\Delta\Omega(r) - \min(\Delta\Omega)}{\max(\Delta\Omega) - \min(\Delta\Omega)} - \frac{1}{2}. \tag{18}$$

The shape function $\psi(r)$ is normalized to vary between $-1/2$ where $\Delta\Omega$ obtains its minimum value (always in the RZ) and $+1/2$ where $\Delta\Omega$ obtains its maximum value (always in the CZ). We define a given tachocline's centroid r_t and thickness Γ as the parameters in the function $(1/2)\tanh[2(r-r_t)/\Gamma]$ which is the best fit to $\psi(r)$.[2]

Figure 5 shows the ψ profiles for the Sun and some medium- and strong-field cases, along with the corresponding best-fit tanh functions. As we would expect,

---

[2] This fitting procedure is similar to (though not as involved as) conventional tachocline fitting methods (e.g., Charbonneau et al. 1999; Basu & Antia 2003). We do not feel our simulated rotation profiles are sufficiently solar-like to warrant more complex fitting.

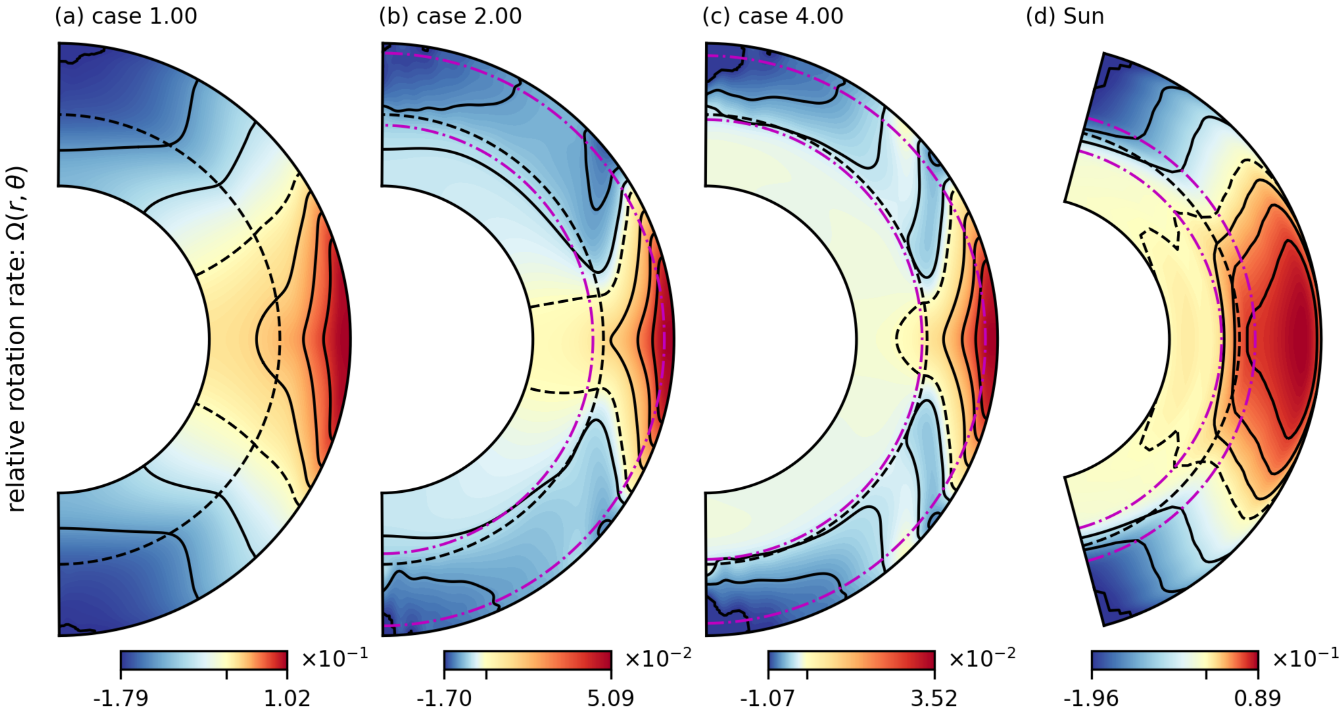

Figure 3. Relative rotation rate Ω for (a)–(c) simulations in each of the three dynamo regimes and (d) the Sun, plotted in color in the meridional plane. Each colormap is bi-linear: positive values (red tones) are normalized separately from negative values (blue tones). The minimum and maximum saturation ticks are labeled on the colorbar, while the zero tick is unlabeled. Overplotted, there are three equally-spaced positive and negative solid contours. The zero contour is dashed. The dashed black curves shows the location of r_0 and for (b)–(d), the dash-dotted magenta curves show the boundaries of the tachocline, $r_t \pm \Gamma/2$. The solar rotation rate is from a helioseismic inversion of GONG data averaged from 1995 to 2009 (Howe et al. 2005; Howe 2023). To arrive at the non-dimensional, relative rotation rate Ω for the Sun, we define $\Omega_\odot \equiv 2.70\times10^{-6}$ rad s^{-1} (or $\Omega_\odot/2\pi = 430$ nHz), which is roughly the solid-body rotation rate of the solar RZ. We then subtract $\Omega_\odot$ from the inverted rotation rate (which is given dimensionally, in the non-rotating frame) and divide by $\Omega_\odot$.

the solar ψ (or best-fit tanh) profile has a centroid near $r = r_0$ and a relatively narrow width. For each simulated tachocline, the distributed radial shear in the CZ both widens the ψ (or tanh) profile and pushes its centroid close the middle of the CZ.

Table 3 shows the tachocline parameters, as well as $\Delta\Omega_{\rm CZ}$, $\Delta\Omega_{\rm RZ}$, f, and $\Omega_{\rm RZ}$ for our simulations and the Sun. Clearly stronger fields reduce rotation contrast everywhere, but significantly more so in the RZ. Interestingly, the "tachocline contrast ratio" f is a non-monotonic function of regime and appears to be minimized (to a value of roughly 0.11) near $\mathrm{Pr_m} = 4$. The nominal solar value is quite a bit higher: $f_\odot \sim 0.3$ from Table 3. However, this is mostly due to the uncertain tachocline width. The solar "$\Delta\Omega_{\rm RZ}$" thus contains substantial contrast from the lower half of the tachocline. Deeper in the RZ ($r/R_\odot \lesssim 0.6$) the helioseismic inversion gives $\Delta\Omega \sim 0.014$ or $f_\odot \sim 0.07$, which is probably closer to the value simulations should tend towards to be considered sufficiently solar-like.

In contrast to the Sun, all the simulated tachoclines have centroids well within the CZ, and are roughly twice as thick. There is no clear scaling of the tachocline centroid with regime. However, the tachoclines in the strong-field regime appear ever so slightly thinner than the tachoclines in the medium-field regime. Overall, it does not seem that further increasing the magnetic field strength will push the tachoclines to be more solar-like. Furthermore, there does not appear to be a solar-like "sweet spot" (say, in between the medium- and weak-field regimes), wherein the RZ rotates like a solid body, but strong rotation contrast is sustained in the CZ.

4.2. *Torque Balance*

In Paper I, we explicitly showed that the magnetic torque from the cycling, non-axisymmetric dynamo field was responsible for confining the tachocline in case 4.00. This remains true for all the medium- and strong-field cases here. In the equilibrated state, the zonally and temporally averaged ϕ-component of the momentum

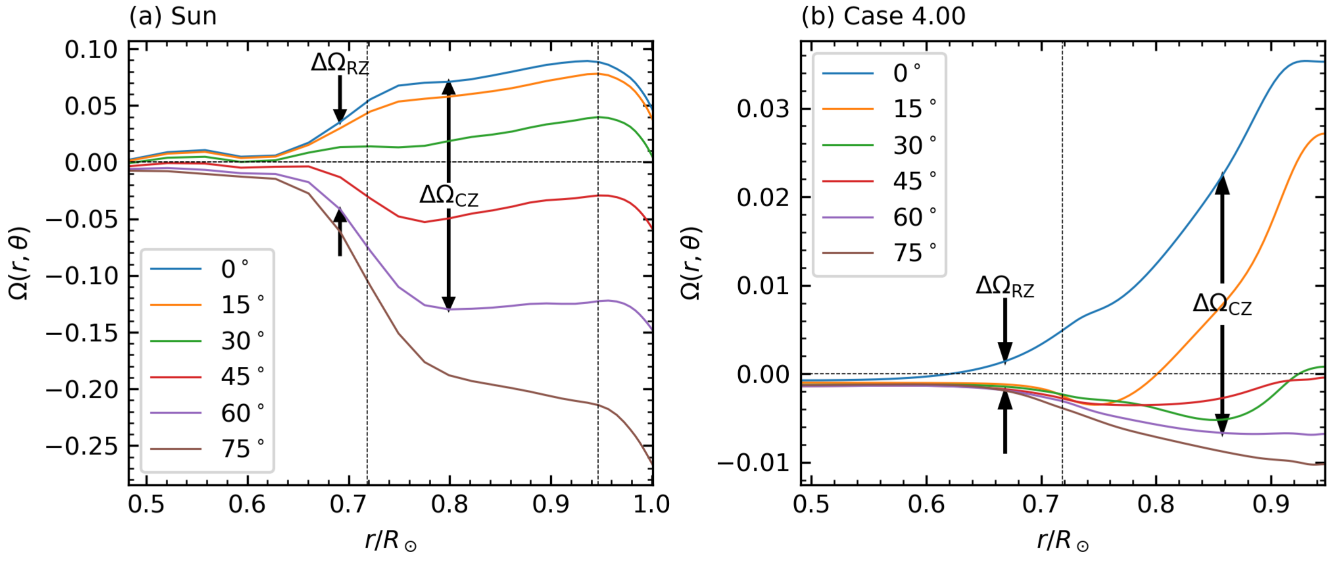

Figure 4. Rotation rate $\Omega(r,\theta)$, plotted along radial lines for (a) the Sun and (b) the strong-field case 4.00. Six radial cuts of Ω are plotted, equally spaced in latitude by 15° between 0° and 75°. In panel (a), the x-axis is extended slightly, since the simulations only extend to $r_{\rm out} = 0.947R_\odot$. In both panels, the vertical arrows represent the values of $\Delta\Omega_{\rm RZ}$ and $\Delta\Omega_{\rm CZ}$. In this figure (and in all radial plots in subsequent figures), the thin vertical lines denote the locations of r_0 and $r_{\rm out}$.

Table 3. Properties of the rotation rate for our simulations and the Sun. Properties for the weak-field cases are not shown, since they are almost identical to case H. . Note that for the Sun, we have $r_{t,\odot}/R_\odot = 0.71$ and $\Gamma_\odot/R_\odot = 0.11$, in reasonable agreement with the helioseismic estimates given in Section 1.

Case	H	1.08	1.33	1.67	2.00	3.00	4.00	6.00	8.00	Sun
regime	-	M	M	M	M	S	S	S	S	-
$\Delta\Omega_{\rm CZ}$	0.192	0.057	0.045	0.041	0.041	0.030	0.027	0.024	0.022	0.199
$\Delta\Omega_{\rm RZ}$	0.116	0.016	0.011	9.13e-3	9.34e-3	3.34e-3	2.56e-3	2.57e-3	2.36e-3	0.046
$f \equiv \Delta\Omega_{\rm RZ}/\Delta\Omega_{\rm CZ}$	0.603	0.287	0.239	0.221	0.227	0.112	0.094	0.106	0.108	0.232
$\Omega_{\rm RZ}$	-0.025	-4.33e-3	-2.91e-3	-2.55e-3	-2.55e-3	-1.42e-3	-1.26e-3	-1.19e-3	-1.11e-3	-3.85e-3
$r_t/R_\odot$	-	0.073	0.082	0.085	0.083	0.087	0.087	0.081	0.076	-8.67e-3
$\Gamma/R_\odot$	-	0.247	0.234	0.226	0.229	0.209	0.203	0.199	0.201	0.111

Equation (8) yields

$$\underbrace{-\nabla\cdot\left[\overline{\rho}r\sin\theta\left\langle u'_\phi\boldsymbol{u}'_{\rm pol}\right\rangle_{\phi,t}\right]}_{\tau_{\rm rs}\ \text{(Reynolds stress)}} - \underbrace{\overline{\rho}\left\langle\langle\boldsymbol{u}_{\rm pol}\rangle_\phi\cdot\nabla\mathcal{L}\right\rangle_t}_{\tau_{\rm mc}\ \text{(meridional circulation)}} + \\ +\underbrace{{\rm Ek}\nabla\cdot\left[\overline{\rho\nu}r^2\sin^2\theta\nabla\Omega\right]}_{\tau_{\rm v}\ \text{(viscous)}} + \underbrace{\nabla\cdot\left[r\sin\theta\left\langle B'_\phi\boldsymbol{B}'_{\rm pol}\right\rangle_{\phi,t}\right]}_{\tau_{\rm ms}\ \text{(Maxwell stress)}} \\ +\underbrace{\nabla\cdot\left[r\sin\theta\left\langle\langle B_\phi\rangle_\phi\langle\boldsymbol{B}_{\rm pol}\rangle_\phi\right\rangle_t\right]}_{\tau_{\rm mm}\ \text{(mean magnetic)}} = 0, \tag{19a}$$

$$\text{where}\qquad \underbrace{\mathcal{L}\equiv r\sin\theta(r\sin\theta+\langle u_\phi\rangle_\phi)}_{\text{angular momentum density}}, \tag{19b}$$

where for a vector field $\boldsymbol{A}$ we define its poloidal component $\boldsymbol{A}_{\rm pol}\equiv A_r\hat{\boldsymbol{e}}_r+A_\theta\hat{\boldsymbol{e}}_\theta$. The torques can be attributed to the physical processes labeled underneath each term (see Miesch & Hindman 2011; Matilsky et al. 2019).

Figure 6 shows the full steady-state torque balance (in the CZ and RZ separately) for case 1.06 (the strongest weak-field case) and the strong-field case 4.00. The CZ of case 1.06 [Figure 6(a)] is effectively hydrodynamic in its torque balance. It represents the "standard" by which current global models (e.g., Hotta et al. 2015; Guerrero et al. 2016; Matilsky et al. 2019) maintain a solar-like differential rotation with fast equator and slow pole. That is, the rotational influence on the convection lead to Taylor columns with correlations in $\boldsymbol{u}$ (i.e., Reynolds stresses), which transport angular momentum away from the rotation axis and produce mostly positive torques at low latitudes ($\lesssim 45°$; further from the rotation axis) and negative torques at high latitudes ($\gtrsim 45°$; closer to the rotation axis). Meridional circu-

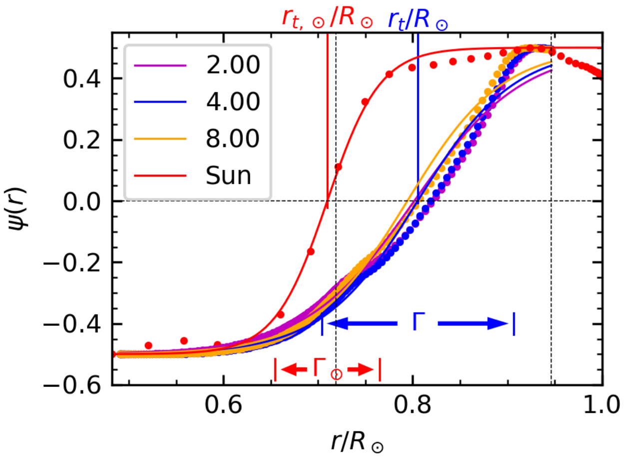

Figure 5. Scatter plots showing the ψ profiles (Equation (18)) for a weak-, medium-, and strong-field case, as well as the Sun. Corresponding line plots show the function $(1/2)\tanh[2(r-r_t)/\Gamma]$ which is the best fit to ψ. Various lines and arrows indicate the values of r_t and Γ for case 4.00 and the Sun.

lation also plays a role (a complicated one due to the presence of multiple circulation cells), especially at low latitudes. Viscosity always tries to eliminate gradients in Ω, in this case the latitudinal gradients, by spinning the equator down and the polar regions up. The RZ of case 1.06 [Figure 6(b)] has a torque balance that is roughly an imprint of the balance in the CZ, but is overall much weaker and concentrated at high latitudes (and the magnetic torques are negligible).

The torque balance in the CZ of case 4.00 [Figure 6(c)] still has a positive Reynolds stress torque, but confined to significantly lower latitudes $\lesssim 15^\circ$. Consequently, most differential rotation is confined to a narrow prograde jet at the equator. The Maxwell-stress torque opposes the Reynolds-stress torque and effectively acts as an additional source of viscous torque. The meridional-circulation torque is significantly altered from its weak-field counterpart as well. Evidently, strong-field magnetism not only provides an additional torque, but also changes the structure of the convection and circulation so as to alter the hydrodynamic torques from their weak-field forms.

Finally, the RZ of case 4.00 [Figure 6(d)] was studied in Paper I and clearly is the balance responsible for tachocline confinement. The profile of viscous torque has changed sign compared to the other figure panels: it is now positive at low latitudes ($\lesssim 15^\circ$) and negative at high latitudes ($\gtrsim 15^\circ$), thus trying to imprint the equatorial jet and weak high-latitude retrograde differential rotation downward.[3] The viscous torque is countered by the magnetic torque, which must come from the large-scale, non-axisymmetric ($m = 1, 2$) field components shown in Figure 2 (that this is true, at least for case 4.00, was shown explicitly in Paper I).

All our weak- and strong-field cases have torque balances like those in Figure 6. The medium-field cases have balances essentially similar to the strong-field cases, but the torques become more complicated due to the intermittent changes in field strength and differential rotation that was noted in connection with Figure 1. Regardless, the answer to how our simulated tachoclines are confined reduces to explaining the maintenance of large-scale, non-axisymmetric magnetism in the RZ. The following sections show how this maintenance can be understood in terms of the cycling dynamo and skin effect.

5. CYCLING BEHAVIOR

5.1. *Dynamo Cycles in the Weak- and Strong-Field Regimes*

Figure 7 (left-hand panels) shows time-latitude diagrams of $\langle B_\phi\rangle_\phi$ for the weak-field case 1.00 and real$(B_{\phi,1})$ for the strong-field case 4.00 at two depths, one in the CZ and one in the RZ. Both cases cycle, although the polarity reversals in the weak-field case occur significantly more regularly than the reversals in the strong-field case. In each case, the cycle "imprints" from the base of the CZ onto the RZ with a phase lag (i.e., for every reversal in the CZ, there is a corresponding reversal in the RZ some time later). There is also significantly more rapid variation in the large-scale field in the CZ (seen as graininess in the time-latitude plots) than in the RZ. This again suggests that the RZ acts as a low-pass filter, in time as well as in space.

To describe these cycles more precisely, we define the frequency components of each $\boldsymbol{B}_m$:

$$\boldsymbol{B}_{m\omega} \equiv \left\langle \boldsymbol{B}_m e^{i\omega t} W(t)\right\rangle_t = \left\langle \boldsymbol{B} e^{-i(m\phi-\omega t)} W(t)\right\rangle_{\phi,t}, \tag{20}$$

where $W(t)$ is the Hanning window function and ω is the discrete angular frequency. From the convention in the exponential (for nonzero m only), the $\boldsymbol{B}_{m\omega}$ components with positive ω/m move prograde in longitude and the components with negative ω/m move retrograde.

---

[3] Note that the viscous torque always attempts to eliminate gradients in Ω; however, in the presence of other torques, it cannot eliminate the gradient in all directions. In the case of a radial shear layer like the tachocline, viscosity will reduce $|\partial\Omega/\partial r|$ at the expense of imprinting the latitudinal differential rotation downward, which of course increases $|\partial\Omega/\partial\theta|$.

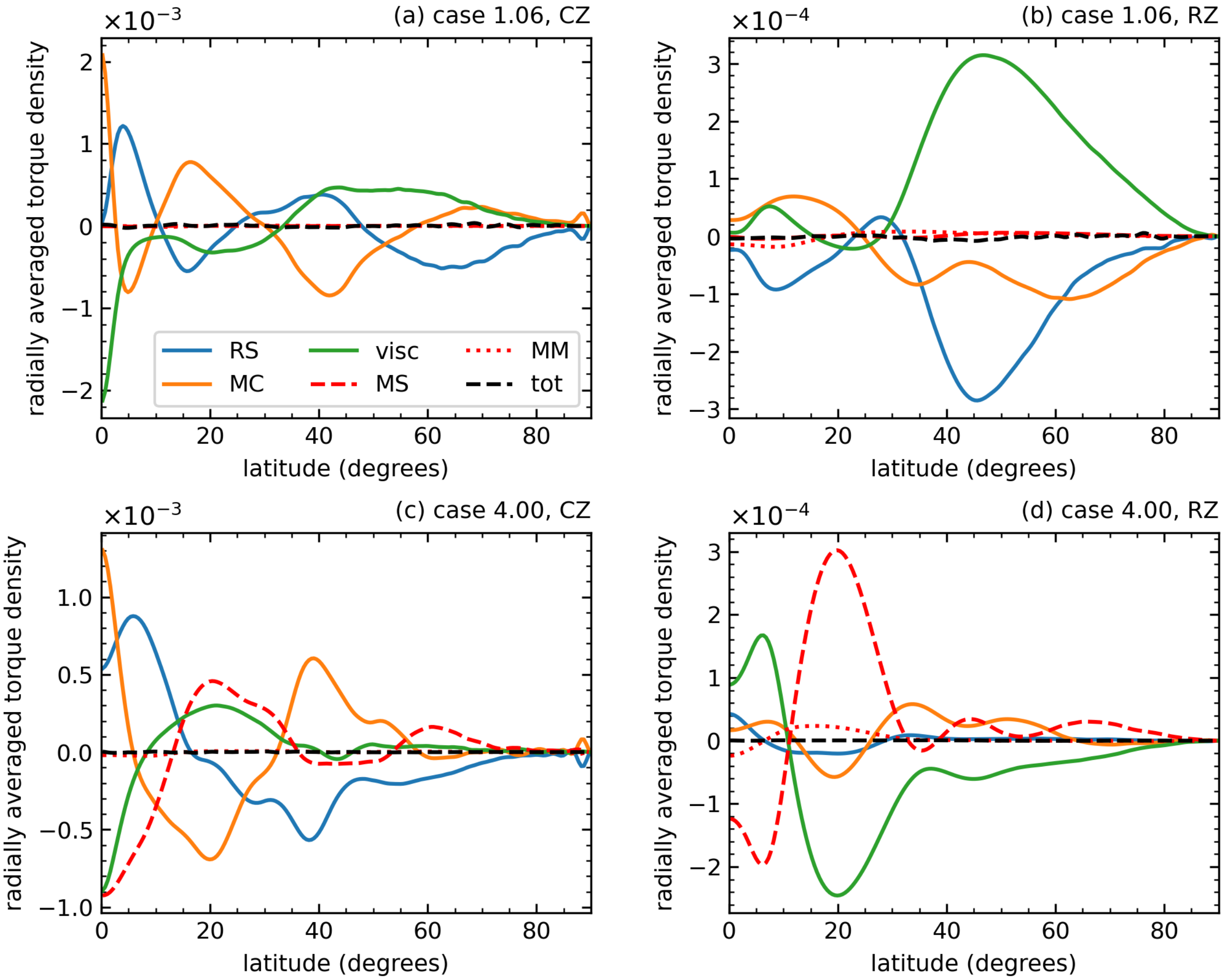

Figure 6. Torque densities, temporally averaged over the equilibrated state. The torques are also radially averaged, separately for the CZ (left column) and RZ (right column), and the equatorially symmetric parts are plotted as functions of latitude for the weak-field case 1.06 (top row) and strong-field case 4.00 (bottom row). The abbreviations in the legend shows which torque density from Equation (19) is plotted: Reynolds stress (RS), meridional circulation (MC), viscous (visc), Maxwell stress (MS), mean magnetic (MM), or total (tot).

We sample the spherical-slice magnetic-field data during the equilibrated state ($t_{\rm eq}$ to $t_{\rm max}$). The sampling intervals are not uniform within a given simulation, but they are typically close to the mean interval $\delta t\sim 3$–$4P_{\rm rot}$, with a typical standard deviation of $\sigma_t\sim 0.1$–$0.4P_{\rm rot}$ (see Table 4). We thus interpolate the non-uniform time series onto a uniform time series spaced by δt before computing the (windowed) discrete Fourier transform represented by Equation (20).

Figure 7 (right-hand panels) shows the power in the large-scale toroidal field ($|B_{\phi,0\omega}|^2$ for the weak-field case and $|B_{\phi,1\omega}|^2$ for the strong-field case) corresponding to the time-latitude diagrams. The regularity of the weak-field cycle causes most of the power to be concentrated in the primary central frequency. By contrast, for the irregular strong-field cycle, there is a wide dispersion of power around a negative central frequency. This preference for negative frequencies suggests retrograde propagation of $\boldsymbol{B}_1$, broadly consistent with transport by the negative background rotation rate in the RZ. Furthermore, the high-$|\omega|$ "tail" in the strong-field case is significantly less pronounced in the RZ than in the CZ, again reinforcing the idea that the RZ acts as a low-pass filter in time.

Figure 7 (right-hand panels) shows that in each case, there is a central frequency (the "primary" cycle frequency $\omega_{\rm cyc}$) and a dispersion (of width σ_ω) in power about this central frequency. More precisely, for a given powerspectrum $P(\omega)$, we define $\omega_{\rm cyc}$ as the median frequency associated with $P(\omega)$ and σ_ω as $P(\omega)$'s half-

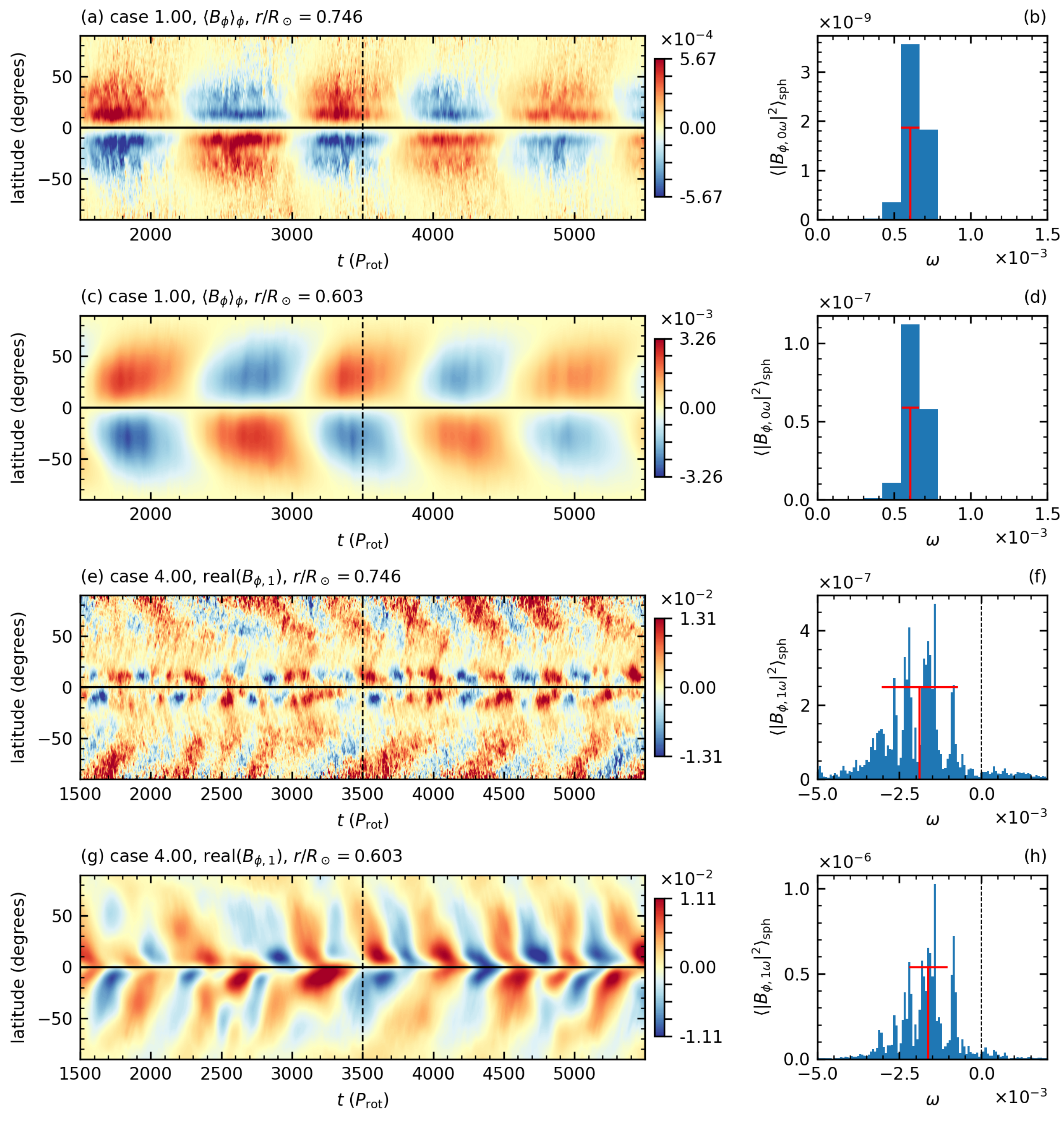

Figure 7. Time-latitude diagrams of the large-scale ($m = 0$ or 1) toroidal field over the interval $(1500, 5500)P_{\rm rot}$ for a weak-field, axisymmetric dynamo (case 1.00; upper 4 panels) and a strong-field, non-axisymmetric dynamo (case 4.00; lower 4 panels). For each case, we sample the same two depths as Figure 2. The horizontal solid line marks the equator and the vertical dashed line marks $t = 3500\ P_{\rm rot}$, the instant sampled by Figure 2. To the right of each time-latitude diagram, we show (for the same depth and m-value as the time-latitude plot) the latitudinally averaged toroidal-field powerspectrum $P(\omega) = \left\langle |B_{\phi,m\omega}|^2 \right\rangle_{\rm sph}$ [see Equation (20); here, m is 0 or 1]. Since $\boldsymbol{B}_0 = \langle \boldsymbol{B} \rangle_\phi$ is real, we consider $P(\omega)$ a function of positive ω only when $m = 0$. The red "T" marks the location of the primary cycle frequency $\omega_{\rm cyc}$ and the dispersion σ_ω for $P(\omega)$ [see Equation (21)]. For case 4.00 (panels f,h), $\omega = 0$ is marked by a vertical dashed line.

Table 4. Dynamo cycle properties for each magnetic case ($\omega_{\rm cyc}$, σ_ω, $P_{\rm cyc}$, and q), as defined in Equation (21). Here, δt and σ_t are the mean and standard deviation in the sample rate for the spherical-slice magnetic field data, $\omega_{\rm nyq} \equiv 2\pi/(2\delta t)$ is the (angular) Nyquist frequency, and $\delta\omega \equiv 2\pi/(t_{\rm max} - t_{\rm eq})$ is the (angular) frequency resolution.

Case	1.00	1.05	1.06	1.08	1.33	1.67	2.00	3.00	4.00	6.00	8.00
Regime	W	W	W	M	W	M	M	M	S	S	S
$\omega_{\rm cyc}$	6.07e-4	5.80e-4	5.20e-4	-5.21e-3	1.56e-3	-4.65e-3	-5.13e-3	-2.52e-3	-1.74e-3	-1.45e-3	-1.52e-3
$P_{\rm cyc}/P_{\rm rot}$	1648	1724	1923	191.9	642.2	215.1	194.9	396.1	574.1	692.0	656.9
σ_ω	9.97e-5	1.62e-4	2.89e-4	3.52e-3	2.47e-3	7.35e-3	0.011	3.71e-3	1.74e-3	1.86e-3	9.51e-4
$q \equiv \omega_{\rm cyc}/\sigma_\omega$	6.09	3.57	1.80	1.48	0.63	0.63	0.46	0.68	1.00	0.78	1.60
$\delta t/P_{\rm rot}$	3.76	3.79	3.76	4.10	4.08	4.03	3.95	3.53	3.18	2.87	2.65
$\sigma_t/P_{\rm rot}$	0.40	0.37	0.37	0.08	0.08	0.14	0.21	0.30	0.25	0.17	0.14
$\omega_{\rm nyq}$	0.133	0.132	0.133	0.122	0.122	0.124	0.127	0.141	0.157	0.174	0.189
$\delta\omega$	1.21e-4	1.93e-4	1.73e-4	1.41e-4	1.73e-4	1.50e-4	1.25e-4	1.49e-4	6.97e-5	2.06e-4	1.90e-4

integral width:

$$\sum_{\omega \le \omega_{\rm cyc}} P(\omega) = \sum_{\omega=\omega_{\rm cyc}-\sigma_\omega/2}^{\omega_{\rm cyc}+\sigma_\omega/2} P(\omega) \equiv \frac{1}{2}\sum_{\omega} P(\omega). \quad (21)$$

The cycle period is $P_{\rm cyc} \equiv 2\pi/\omega_{\rm cyc}$ (since $P_{\rm rot} = 2\pi$, note that $P_{\rm cyc}/P_{\rm rot} = 1/\omega_{\rm cyc}$). The quantity $q \equiv \omega_{\rm cyc}/\sigma_\omega$ defines the regularity of the cycle, with higher q indicating a more regular cycle.

Table 4 contains values of $\omega_{\rm cyc}$, $P_{\rm cyc}$, σ_ω, and q, along with the sampling parameters δt, Nyquist frequency $\omega_{\rm nyq}$, and frequency resolution $\delta\omega$. For the weak-field cases, we take $P(\omega) = \left\langle |\boldsymbol{B}_{0\omega}|^2 \right\rangle_{\rm full}$ (considering positive ω only, since $\boldsymbol{B}_0 = \langle \boldsymbol{B} \rangle_\phi$ is real) and for the non-weak-field cases, we take $P(\omega) = \left\langle |\boldsymbol{B}_{1\omega}|^2 \right\rangle_{\rm full}$ (considering both positive and negative ω). The weak-field solutions all have similar cycle periods ($P_{\rm cyc} \sim 1400$–$2000 P_{\rm rot}$), with relatively high values of q, about equal to the number of cycles contained in the full run. This confirms the visual appearance of regular cycles in the weak-field cases (Figure 7).

The medium- and strong-field cases have more irregular cycles (with $q \lesssim 1$) and the cycle period (with the exception of either one of cases 1.67 or 2.00) monotonically increases with increasing field strength. Since field strength increases with $\mathrm{Pr_m}$ and therefore with magnetic diffusion time P_η (see Table A1), this suggests that the cycle period for the non-weak cases is at least partly determined by the level of diffusion (i.e., $P_{\rm cyc}$ scales more or less monotonically with P_η).

6. SKIN-DEPTH INTERPRETATION

As mentioned at the conclusion of Section 4.2, explaining the presence (or not) of tachoclines in these simulations boils down to the maintenance of large-scale ($m = 1, 2$) $\boldsymbol{B}_{\rm pol}$ in the RZ.[4] In Paper I, we showed that two effects were responsible for this maintenance: induction (possibly from inertial oscillations) and diffusion of CZ-produced field to roughly a (then ill-defined) skin-depth below the CZ. In this section, we precisely define the relevant skin effect and we show how the amplitude of $\boldsymbol{B}_{\rm pol}$ in the RZ can be extremely well-predicted considering only diffusive skin effects.

As a first approximation, we assume that fluid motions produce no electromotive force (e.m.f.) below r_0 (or a radius slightly below r_0 for the weak-field cases; see Figure 8's caption). Then the evolution of $\boldsymbol{B}_{\rm pol}$ in the RZ is governed by diffusion alone, with the upper boundary condition (at $r = r_0$) that $\boldsymbol{B}_{\rm pol}$ matches what the CZ produces and the lower boundary condition (at $r = r_{\rm in}$) that the field decays to near-zero. For axisymmetric weak-field dynamos, the regular polarity reversals provide an oscillating boundary condition at a single frequency. This is the classic form of Stokes' problem (of an oscillating boundary) and the field amplitude is contained in an envelope that decays exponentially downwards with a scale height (in this context, called the skin depth) that depends on the frequency of oscillation. This is the formalism expounded in the original "fast magnetic confinement" theory of Forgács-Dajka & Petrovay. In the axisymmetric case, the rotation rate of the frame in which the equations are solved does not matter.

However, for the non-axisymmetric medium- and strong-field dynamos, the choice of rotating frame does matter. Since advection in ϕ of a non-axisymmetric $\boldsymbol{B}_{\rm pol}$ constitutes an e.m.f., diffusion-only evolution is possible only if the RZ rotates approximately like a solid body. To examine purely diffusive solutions, the induction equation must be written in the frame rotating at the solid-body rate $\Omega_{\rm RZ}$ (see Table 3 for the simulated and solar values of $\Omega_{\rm RZ}$). Because the field at $r = r_0$ is cycling with multiple frequencies (see the previous Section 5), this setup still corresponds to Stokes' problem, but there is now a different skin-depth for each component $\boldsymbol{B}_{{\rm pol},m\omega}$. Furthermore, since the equations must be solved in the frame of the RZ, the frequency determining the skin-depth is not ω, but the "Doppler-shifted" value $\omega - m\Omega_{\rm RZ}$.[5]

Assuming that the spatial variation of $\boldsymbol{B}_{\rm pol}$ is predominantly radial, Equation (10) leads to separate boundary-value problems for each $\boldsymbol{B}_{{\rm pol},m\omega}$:

$$-i(\omega - m\Omega_{\rm RZ})\boldsymbol{B}_{{\rm pol},m\omega} \approx \frac{\rm Ek}{\rm Pr_m}\overline{\eta}(r)\frac{\partial^2 \boldsymbol{B}_{{\rm pol},m\omega}}{\partial r^2} \quad (22)$$

for $r \le r_0$. Rapid variation in r allows us to neglect the terms in ∇^2 other than $(\partial/\partial r)^2$, sphericity terms, and the term from $\nabla\overline{\eta}$. Note that Equation (22) is valid for all m.

Because $\overline{\eta}(r)$ varies with radius, we follow Garaud (1999) and define

$$r_\eta \equiv r_{\rm in} + \frac{\int_{r_{\rm in}}^{r} \overline{\eta}(r')^{-1/2} dr'}{\int_{r_{\rm in}}^{r_0} \overline{\eta}(r')^{-1/2} dr'}. \quad (23)$$

---

[4] Maintenance of large-scale B_ϕ is also important of course. However, if $\boldsymbol{B}_{\rm pol}$ is present, B_ϕ is always created by mean shear. In Paper I, we argued that this effect—similar in essence to Ferraro's law (Ferraro 1937)—is in fact responsible for the magnetic torque and hence tachocline confinement. In this work, we thus only consider the maintenance of $\boldsymbol{B}_{\rm pol}$.

[5] Note that the relative signs of ω and $\Omega_{\rm RZ}$ matter here, but the sign of $\omega - m\Omega_{\rm RZ}$ does not; see Equation (25b).

Note that r_η is a monotonically increasing function of r and is equal to r at $r = r_{\rm in}$ and $r = r_0$.[6] Again assuming rapid radial variation, Equation (22) becomes

$$-i(\omega - m\Omega_{\rm RZ})\boldsymbol{B}_{{\rm pol},m\omega} \approx \frac{\rm Ek}{\rm Pr_m}\overline{\eta}_{\rm const}\frac{\partial^2 \boldsymbol{B}_{{\rm pol},m\omega}}{\partial r_\eta^2}, \quad (24a)$$

$$\text{where} \quad \overline{\eta}_{\rm const} \equiv \left[\frac{r_0 - r_{\rm in}}{\int_{r_{\rm in}}^{r_0}\overline{\eta}(r')^{-1/2}dr'}\right]^2 \quad (24b)$$

is an intermediate value of $\overline{\eta}(r)$ in the RZ. For our chosen reference state, $\overline{\eta}_{\rm const} = 0.292$ and $\overline{\eta}(r)$ achieves this value at $r/R_\odot = 0.599$.

Equation (24) is of course Stokes' problem again and its exact solution yields

$$\left\langle|\boldsymbol{B}_{{\rm pol},m\omega}|^2\right\rangle_{\rm sph}(r) = \left\langle|\boldsymbol{B}_{{\rm pol},m\omega}|^2\right\rangle_{\rm sph}(r_0)\times \exp\left[-2\left(\frac{r_0 - r_\eta}{\delta_{m\omega}}\right)\right], \quad (25a)$$

$$\text{where} \quad \delta_{m\omega} \equiv \sqrt{\frac{2{\rm Ek}\overline{\eta}_{\rm const}}{{\rm Pr_m}|\omega - m\Omega_{\rm RZ}|}} \quad (25b)$$

is the m- and ω-dependent skin-depth.

The "skin-predicted" amplitude of large-scale $\left\langle|\boldsymbol{B}_{\rm pol}|^2\right\rangle_{{\rm sph},t}$ is then found by summing Equation (25) over all ω and low m: we choose $m = 0$ for the weak-field cases and $m \in \{0, 1, 2\}$ for the medium- and strong-field cases. Figure 8 shows large-scale $\left\langle|\boldsymbol{B}_{\rm pol}|^2\right\rangle_{{\rm sph},t}$ (both the skin-predicted and actually-realized values) for a weak-, medium-, and strong-field case. Equation (25) does an extremely good job of predicting the field strength for the weak- and strong-field cases and a reasonable job for the medium-field case. Overall, it thus seems highly likely that the magnetization of the RZ is determined primarily by the dynamo cycle of the CZ imprinting diffusively downward.

In Paper I, the strong $\boldsymbol{B}_{\rm pol}$ in the RZ of case 4.00 was attributed partially to deep dynamo action. For all the magnetic cases considered here, we have verified that the deep dynamo is still present, that is, the production of $|\boldsymbol{B}_{\rm pol}|^2$ by diffusion ($D_{\rm pol}$) is negative in the RZ, while the production by e.m.f. ($I_{\rm pol}$) is positive.[7] It was emphasized in Paper I that this implies (by definition; e.g., Moffatt & Dormy 2019, p. 146) the presence of dynamo action deep in the RZ, and we argued that this deep dynamo (possibly driven by Rossby waves) may have been responsible for tachocline confinement in case 4.00. However, the results of this section indicate that the strength of $\boldsymbol{B}_{\rm pol}$ in the medium- and strong-field cases can be almost fully accounted for by diffusive skin effects. It thus seems likely we would have tachocline confinement (in the simulations considered here) regardless of whether there was a deep dynamo or not. How the deep dynamo is driven—and whether it *can* confine the tachocline in the absence of large diffusion—remains an intriguing open question.

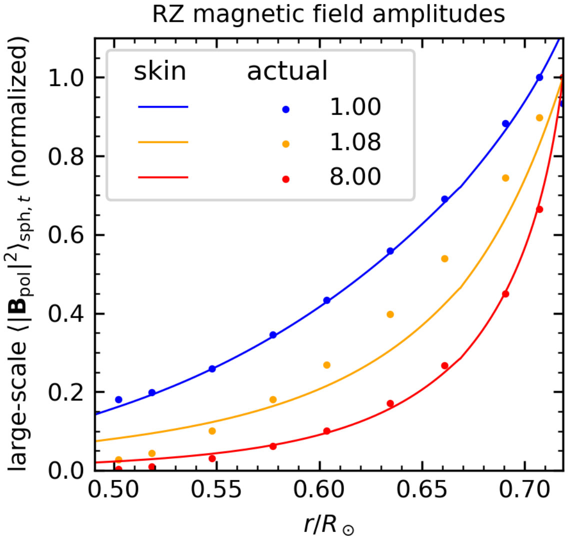

Figure 8. Amplitude (in the RZ) of "large-scale $\left\langle|\boldsymbol{B}_{\rm pol}|^2\right\rangle_{{\rm sph},t}$", defined here as $\sum_m \left\langle|\boldsymbol{B}_{{\rm pol},m}|^2\right\rangle_{{\rm sph},t}(r)$, where the sum is over $m = 0$ for weak-field cases and $m \in \{0, 1, 2\}$ for medium- and strong-field cases. We show both the actual amplitude (solid dots) and the amplitude predicted by the skin-depth Equation (25) (solid curves) for cases 1.00, 1.08, and 8.00. For case 1.00, we replace r_0 in Equation (25) with a value r_c slightly below the CZ: $r_c/R_\odot = 0.707$. Each profile is normalized such that its value at $r = r_0$ (or $r = r_c$ for case 1.00) is unity.

7. POLARITY REVERSALS FOR NON-AXISYMMETRIC MAGNETIC FIELDS

Polarity reversals in non-axisymmetric magnetic fields [e.g., Figures 7(e,g)] can be accomplished in two distinct ways. For definiteness, consider $B_{\phi,1}$ (i.e., the colatitudinal field associated with a single partial-wreath pair). At a given radius and latitude, we have

$$B_{\phi,1}(t) = \sum_\omega B_{\phi,1\omega}e^{-i\omega t} = A(t)e^{i\varphi(t)} \quad (26)$$

The first type of reversal is due to modulation of the amplitude $A(t)$. These reversals contain cycle minima [for which $A(t) = 0$] and are analagous to the reversals

---

[6] We believe that the r_η given in Garaud (1999), which had $\overline{\eta}(r')^{+1/2}$ in the integrand in the analog of Equation (23), was mistakenly defined.

[7] Explicitly, we define $D_{\rm pol}(r) \equiv \left\langle\boldsymbol{B}_{\rm pol}\cdot[\nabla\times(\overline{\eta}\nabla\times\boldsymbol{B})]_{\rm pol}\right\rangle_{{\rm sph},t}$ and $I_{\rm pol}(r) \equiv \left\langle\boldsymbol{B}_{\rm pol}\cdot[\nabla\times(\boldsymbol{u}\times\boldsymbol{B})]_{\rm pol}\right\rangle_{{\rm sph},t}$. We have verified that in all magnetic cases, at all radii in the RZ, $D_{\rm pol}(r) < 0$, while $I_{\rm pol}(r) > 0$.

of the full-wreath (i.e., axisymmetric) polarities in the weak-field case [Figures 7(a,c)], or equivalently to what we believe happens to the solar interior magnetic field to cause the observed butterfly diagram (e.g., Hathaway 2015). The second type of reversal is due to changes in the phase $\varphi(t)$, which simply occurs from advection of the whole structure in longitude (there are no cycle minima in this case). Equation (26) shows that in general, there is no straightforward way to separate which frequency components $B_{\phi,1\omega}$ are due to each type of reversal. Indeed, in Matilsky & Toomre (2020a) (see Figures 11 and 12 from that paper), we showed that both types of reversal occur simultaneously in the CZ-only partial-wreath cycles, with the frequency of amplitude modulation similar to that of longitudinal advection.

Postponing for now the important investigation of how amplitude modulation occurs (it must be caused by non-axisymmetric dynamo processes; e.g., Stix 1971; Ivanova & Ruzmaikin 1985; Bigazzi & Ruzmaikin 2004; Moss et al. 2002), we discuss in this section which frequencies are consistent with longitudinal advection. Figure 9 shows case 4.00's poloidal powerspectra as functions of latitude and frequency for both $m = 1$ and $m = 2$ at the CZ–RZ interface $r = r_0$. For $m = 1$ (panel a), the shape of the powerspectrum is nearly latitude-independent, with roughly constant values of the latitudinally-dependent cycle frequency $\omega_{\rm cyc}(\theta)$ and dispersion $\sigma_\omega(\theta)$. The central frequency $\omega_{\rm cyc}(\theta)$ overlaps with $m\Omega(r_0, \theta)$ at low latitudes (about 15° north and south), which correspond to the retrograde ($\Omega < 0$) jet of Figure 3(c). For $m = 2$ (panel b), $\omega_{\rm cyc}(\theta) = m\Omega(r_0, \theta)$ at a slightly lower latitude (about 10° north and south) and the dispersion of power $\sigma_\omega(\theta)$ is "stretched" by roughly a factor of two compared to the $\sigma_\omega(\theta)$ for $m = 1$. This stretching factor is consistent with the advective rate being proportional to m-value.

One valid interpretation of Figure 9 is that the large-scale ($m = 1, 2$) structures move as a cohesive structure (i.e., with rotation rates more or less independent of latitude), but at a time-varying rotation rate, which encompasses a range of values $\omega_{\rm cyc} \pm \sigma_\omega/2$ centered about the advective rate $m\Omega(r_0, \theta)$ at low latitudes. Since these low latitudes are also the location of the retrograde jet, we may interpret the partial wreaths as being "anchored" to the jet. Another valid interpretation is that the partial wreaths have an intrinsic rate of rotation caused by the dynamo mechanism, which is seemingly independent of latitude. This dynamo-intrinsic rotation rate then *determines* the rotation rate of the retrograde jet via the magnetic torques (since the magnetic torque should force the fluid to move with $\boldsymbol{B}_{\rm pol}$).

For the skin depth [Equation (25b)], it does not matter which physical process produces a given value of ω. As long as ω is different from $m\Omega_{\rm RZ}$ (see the orange lines in Figure 9), the amplitude of $\boldsymbol{B}_{\rm pol}$ should decay downward with a finite skin-depth. Considering the first interpretation of Figure 9, we thus argue for the relevance of an important new type of skin effect, which arises from non-axisymmetric field at the CZ–RZ interface being advect by a background rotation rate that is different from the rotation rate of the RZ.

One particularly interesting consideration are the latitudes at the base of the CZ that corotate with the RZ. At those latitudes, $\omega - m\Omega_{\rm RZ} = 0$ and the skin-depth in Equation (25b) becomes infinite. What this really means is that any frozen-in non-axisymmetric field appears completely stationary to the RZ and spreads downward indefinitely on a diffusive time-scale. We explore this idea in the solar context in the following section.

8. DISCUSSION: NON-AXISYMMETRIC DYNAMO CONFINEMENT OF THE SOLAR TACHOCLINE

These results suggest that the fast magnetic confinement scenario—which was originally proposed, in 1D only, for axisymmetric $\boldsymbol{B}_{\rm pol}$ cycling at a single frequency (Forgács-Dajka & Petrovay 2001, 2002; Forgács-Dajka 2004; Barnabé et al. 2017)—should be expanded (into 3D) to include both non-axisymmetric $\boldsymbol{B}_{\rm pol}$ and a spread in cycle frequencies. Whether this more general scenario is actually capable of confining the solar tachocline depends on several major differences between simulations and the Sun, which we briefly discuss here. Note that for this section (which is concerned with a real astrophysical object, namely, the Sun), we regard all physical quantities as dimensional.

Prior work on the fast magnetic confinement scenario has always assumed a turbulently enhanced magnetic diffusivity. For example, Barnabé et al. 2017 (see Figure 5 from that paper) nicely show that for dynamo poloidal field strengths of $\sim 10^3$ G (and a cycle period of $\sim$22 yr), the magnetic diffusivity must be larger than its molecular value by a factor of at least 10^5–10^6. However, as discussed in Section 1, how much turbulent enhancement of the viscosity occurs in the hydrodynamic scenario (and if the enhancement is primarily horizontal or vertical) is a subject of ongoing research with no firm conclusions at present. For *magnetic* diffusive enhancement, even less is known. Thus for simplicity, we assume here that the magnetic diffusion is not turbulently enhanced. We also leave aside for now Paper I's proposition that deep dynamo may generate significant $\boldsymbol{B}_{\rm pol}$.

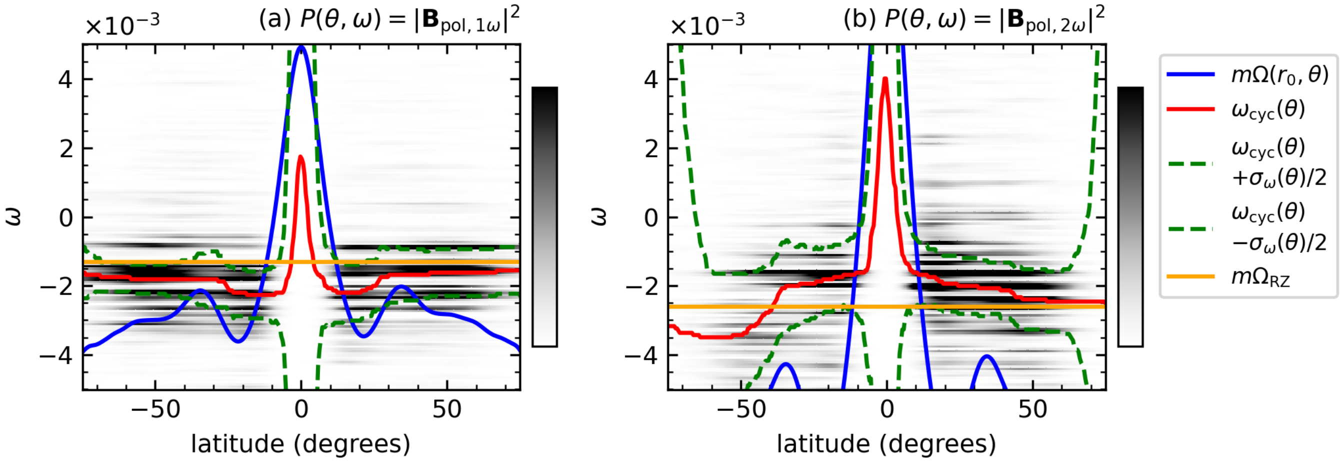

Figure 9. Powerspectra $P(\theta, \omega)$ of the poloidal field at $r = r_0$ in case 4.00 (viewed as functions of latitude and frequency) for (a) $m = 1$ and (b) $m = 2$. Power is shown in gray-scale in arbitrary units (a linear color-scaling is used). Overplotted is the local advective rotation rate $m\Omega(r_0, \theta)$, the location of most of the power [i.e., the θ-dependent values $\omega_{\mathrm{cyc}}(\theta)$ and $\omega_{\mathrm{cyc}}(\theta) \pm \sigma_\omega(\theta)/2$; see Equation (21)], and the advective rotation rate of field in the RZ, $m\Omega_{\mathrm{RZ}}$.

8.1. *Diffusive Equilibration in Simulations*

In the Sun, all diffusive time-scales are signficantly greater than the current solar age ($t_\odot = 4.6$ Gyr; see Table B2). By contrast, the simulations that we are aware of that seek to address the tachocline confinement problem do so by evolving the MHD equations over significant fractions of the relevant diffusion times. If a statistically steady state is achieved, it thus likely contains significant diffusive effects in the dynamical balances.

We believe this may be one of the main reasons our tachocline cases have most of the differential rotation confined to a narrow equatorial jet near the outer boundary. The viscous and magnetic diffusion time-scales are similar (we have order-unity $\mathrm{Pr_m}$ values) and in most cases we run for several of each time-scale. The steady state thus necessarily has similar magnitudes for the viscous and magnetic torques in the CZ and RZ (compare the left-hand and right-hand columns of Figure 6). This means that any magnetic torque strong enough to prevent viscous tachocline spread is also strong enough to eliminate much of the differential rotation in the CZ.

8.2. *Viscous versus Radiative Spread: General Torque Balance*

Even barring the open question of whether circulation burrowing is hyper-diffusive in the Sun, it seems likely that radiative spread dominates viscous spread. This dominance is expressed via the "σ-parameter" (e.g., Garaud & Brummell 2008; Garaud & Acevedo-Arreguin 2009; Wood & Brummell 2012; Acevedo-Arreguin et al. 2013; Wood & Brummell 2018):

$$\sigma \equiv \sqrt{\frac{P_{\mathrm{ES}}}{P_{\nu,\mathrm{RZ}}}} = \frac{\sqrt{\mathrm{PrBu}}}{2} \tag{27}$$

For the Sun, $\sigma_\odot = 0.17 \ll 1$ (see Table B2). Since the Reynolds number in the solar CZ is extremely high, the viscous torque should drop out of the torque balance in the CZ as well. Global simulations seem to indicate that large-scale magnetic field (when strong enough) significantly reduces the differential rotation in the CZ (e.g., Brown et al. 2010; Racine et al. 2011; Passos & Charbonneau 2014; Yadav et al. 2015; Augustson et al. 2015; Guerrero et al. 2019; Bice & Toomre 2020; Matilsky & Toomre 2020a). For a fast magnetic confinement scenario (one in which the dynamo-produced magnetic field diffusively penetrates into the upper RZ) to work, we thus might require that the total magnetic torque ($\tau_{\mathrm{mag}} \equiv \tau_{\mathrm{ms}} + \tau_{\mathrm{mm}}$) be both large enough in the RZ to counter radiative spread and small enough to drop out of the torque balance in the CZ. In that case, Equation (19) becomes

$$0 = \begin{cases} \underbrace{-\dfrac{4\Omega_\odot^2}{N^2} r_0^2 \overline{\rho}\, \overline{\kappa} \dfrac{\partial^4 \langle \mathcal{L} \rangle_t}{\partial r^4}}_{\tau_{\mathrm{rad}}\ \text{(radiative spread)}} + \tau_{\mathrm{mag}} & \text{in the RZ} \\ \tau_{\mathrm{rs}} + \tau_{\mathrm{mc}} & \text{in the CZ,} \end{cases} \tag{28}$$

where the form of τ_{rad} is derived in Spiegel & Zahn (1992) [their Equation (4.9)] and we have assumed a thin tachocline (so that we retain only highest derivatives in r). We estimate $\partial^4 \langle \mathcal{L} \rangle_t / \partial r^4 \sim (r_0/\sqrt{2})^2 \Delta\Omega_{\mathrm{CZ}} / \Gamma_\odot^4$. If we take $\Gamma_\odot = 0.05R_\odot$ and take the Model S values in Table B2 (averaged over the upper solar RZ) for $\overline{\rho}$, $\overline{\kappa}$, and $\overline{N^2}$, and take $\Delta\Omega_{\rm CZ} = 0.20\Omega_\odot$ from Table 3, we find

$$\tau_{\rm mag} \sim \tau_{\rm rad} \sim 0.84 \text{ dyn cm}^{-2} \qquad \text{in the RZ.} \tag{29}$$

Meanwhile in the CZ, the Reynolds stress has not been measured helioseismically (although could be in the future via ring analysis; e.g., Greer et al. 2015, 2016; Nagashima et al. 2020). Nonetheless, the meridional flow's amplitude $|\boldsymbol{u}_{\rm pol}| \sim 10 \text{ m s}^{-1}$ is fairly well known, at least in the upper half of the CZ (e.g., Zhao et al. 2012; Chen & Zhao 2017; Braun et al. 2021) and so we estimate $\tau_{\rm mc} \sim (3/2\pi)\tilde{\rho}|\boldsymbol{u}_{\rm pol}|R_\odot\Delta\Omega_{\rm CZ}$, or

$$\tau_{\rm rs} \sim \tau_{\rm mc} \sim 1.2 \times 10^6 \text{ dyn cm}^{-2} \qquad \text{in the CZ.} \tag{30}$$

Equations (29) and (30) suggest that a diffusively coupled solar CZ and RZ (in which the magnitude of $\tau_{\rm mag}$ is similar in both zones) can support the fast confinement scenario, i.e., $\tau_{\rm rad} \sim \tau_{\rm mag} \ll \tau_{\rm rs} \sim \tau_{\rm mc}$. We can further express $\tau_{\rm mag}$ (as defined in the dimensional form of 28) from the large-scale non-axisymmetric field in terms of field strength: $\tau_{\rm mag} \sim [1/(2\sqrt{2}\pi^2)]|B_\phi|^2$. Here, we have (crudely) assumed that $|\boldsymbol{B}_{\rm pol}| \sim |B_\phi|$, that $r\sin\theta \sim r/\sqrt{2}$, and that the typical length-scale for large-field variation is $\sim\pi r/2$. Equations (29) and (30) then yield

$$4.8\text{G} \lesssim |B_\phi| \ll 5800 \text{ G.} \tag{31}$$

Equation (31) states that if the fast magnetic confinement scenario operates in the Sun, we expect the zonal field strength to be significantly less than 5800 G in the CZ (so as not to disturb the torque balance there) and to diffusively decay to a lower bound of at least 4.8 G in the tachocline region (to counter radiative spread). The value of the lower bound depends strongly on the actual value of $\Gamma_\odot$ and the value of the upper bound on the reliability of the simulations' prediction that strong field quenches differential rotation.[8]

8.3. *Small Skin Depths and Spread of a Permanent Dynamo Field*

Equation (25b) shows that, except for $\omega = m\Omega_{\rm RZ}$, any oscillatory component of the solar dynamo has a very small skin depth and thus cannot significantly penetrate into the RZ (this is the reason why prior 1D models like Barnabé et al. (2017) required an $\overline{\eta}$ greatly enhanced from its molecular value). Explicitly, we rewrite Equation (25b) in dimensional form as

$$\delta_{m\omega} = \left(\frac{2\,\langle\eta\rangle_{\rm RZ}}{|\omega - m\Omega_{\rm RZ}|}\right)^{1/2} = (0.027R_\odot){P_{\rm cyc}}^{1/2}, \tag{32}$$

where here $P_{\rm cyc} \equiv 2\pi/|\omega - m\Omega_{\rm RZ}|$ and is measured in Gyr. If we require diffusive spread over (say) $\Gamma_\odot = 0.05R_\odot$, we need $P_{\rm cyc} \sim 1.4$ Gyr. With the solar age at $t_\odot = 4.6$ Gyr, such a high $P_{\rm cyc}$ cannot unambiguously constitute a "cycle" and instead better corresponds to the permanent component of $\boldsymbol{B}_{\rm pol}$ (as viewed in the frame rotating with the RZ), here denoted $\boldsymbol{B}_{\rm pol,perm}$.[9] There are few, if any, constraints on the solar $|\boldsymbol{B}_{\rm pol,perm}|$, only that it is significantly less than $|\boldsymbol{B}_{\rm pol}|$ (e.g., Usoskin 2013). It is not obvious, however, *how* much less than $|\boldsymbol{B}_{\rm pol}|$ it really is, and thus whether we can rule out a dynamo confinement scenario entirely if $\overline{\eta}$ is not turbulently enhanced.

For example, even if the solar dynamo were purely axisymmetric and perfectly cyclic with a period of 22 yr, we would expect at most $N_{\rm cyc} = (4.6 \text{ Gyr})/(22 \text{ yr}) = 2.1 \times 10^8$ cycles since the dynamo turned on. If we assume there have always been random modulations of the cycle amplitude (as are observed throughout recorded history), then we estimate $|\langle\boldsymbol{B}_{\rm pol,perm}\rangle_\phi| = |\langle\boldsymbol{B}_{\rm pol}\rangle_\phi|/\sqrt{N_{\rm cyc}} = 6.9 \times 10^{-5}|\langle\boldsymbol{B}_{\rm pol}\rangle_\phi|$. Given Equation (31), this reduced field strength would only be a factor of $\sim$10 too small to confine the tachocline.[10]

As noted at the end of Section 7, any non-axisymmetric $\boldsymbol{B}_{\rm pol}$ that co-rotates with the RZ is effectively non-oscillatory and thus contributes to $\boldsymbol{B}_{\rm pol,perm}$. If the fast magnetic confinement scenario is generalized to include non-axisymmetric fields, it thus seems possible that $\boldsymbol{B}_{\rm pol,perm}$ (including all m's) could be significantly larger and more topologically complex than prior estimates like Garaud (1999).

Active longitudes (preferential solar longitudes at which sunspots emerge; e.g., Maunder 1905; Svalgaard & Wilcox 1975; Bogart 1982; Ivanov 2007) are particularly striking as a possible contributor to non-axisymmetric $\boldsymbol{B}_{\rm pol,perm}$. Although it would be a ma-

---

[8] If the large-scale solar magnetic field does *not* quench differential rotation, we would have no reason to expect $\tau_{\rm mag} \lesssim \tau_{\rm mc}$. In fact, the CZ torque balance could be $\tau_{\rm rs} + \tau_{\rm mag} = 0$, in which case $\tau_{\rm mag} \sim \tau_{\rm rs}$, which would be unconstrained until the Reynolds stress is measured.

[9] The discussion here implies that the term "fast" magnetic confinement scenario may be something of an oxymoron; probably "dynamo" confinement scenario would be a more inclusive term.

[10] In other words, from Equation (31), we compute $4.8/5800 = 8.3 \times 10^{-4}$, which is only $\sim$10 times smaller than 6.9×10^{-5}. This estimate also coheres with Garaud (1999), who found an amplitude of $|\langle\boldsymbol{B}_{\rm pol}\rangle_\phi| \sim 0.1$ G in the tachocline region due to "random-walk" diffusive spread.

jor leap to claim that active longitudes imply a permanent interior partial-wreath structure co-rotating with the RZ (authors have done so nonetheless; e.g., Olemskoy & Kitchatinov 2009), it is intriguing that: (1) they often come in opposite-polarity pairs separated in longitude by 180° (e.g., Bai 2003; Mordvinov & Kitchatinov 2004) and (2) they seem to persist, in a properly chosen rotating frame (or in a frame with time-dependent rotation), for long time-scales: 20 years (Henney & Harvey 2002) or even ~100 years (Berdyugina & Usoskin 2003).

Whatever the source of $\boldsymbol{B}_{\rm pol,perm}$, it should penetrate into the RZ much deeper than any skin-depth. Considering the Rayleigh problem (i.e., Stokes' *first* problem, of a boundary plate suddenly jerked from rest), we estimate (for $r \leq r_0$):

$$|\boldsymbol{B}_{\rm pol,perm}|(r) = |\boldsymbol{B}_{\rm pol,perm}|(r_0)\,{\rm erfc}\left(\frac{r_0 - r}{\delta_{\rm perm}}\right), \quad (33)$$

$$\text{where} \qquad \delta_{\rm perm} = \sqrt{4\,\langle\eta\rangle_{\rm RZ}\,t_\odot} = 0.21R_\odot. \quad (34)$$

For $r_0 - r = \Gamma_\odot = 0.05R_\odot$, we find ${\rm erfc}(0.05/0.21) = 0.73$, i.e., there should be only a ~27% reduction in $|\boldsymbol{B}_{\rm pol,perm}|$ over the depth of the tachocline.

8.4. *Conclusion*

In summary, we have performed a suite of dynamo simulations in which tachocline confinement is achieved if the large-scale non-axisymmetric fields (partial wreaths) are strong enough. These partial-wreath structures cycle with frequencies consistent with advection by a low-latitude retrograde jet. The structures thus appear to cycle from the perspective of the rigidly rotating RZ and penetrate diffusively downward, with the amplitude of the confining $\boldsymbol{B}_{\rm pol}$ very well-predicted by the skin-depth Equation (25).

As a whole, the simulations presented here effectively achieve a fast magnetic confinement scenario, which is now generalized to include non-axisymmetric fields and a spread in cycle frequencies. This work thus offers a significantly wider range of applicability to the fast confinement scenario. To further constrain if such a scenario were consistent with observations, we might recommend that future work explore in greater detail the processes giving rise to non-axisymmetric field (such as active longitudes), and determine observationally how fast these structures rotate with respect to the RZ.

In this discussion section, we have argued that if the magnetic diffusivity is not enhanced, then only an effectively permanent component of the solar dynamo can play a role in tachocline confinement. This component can include both the axisymmetric dynamo field (averaged in time since the birth of the Sun) and, possibly more importantly, any non-axisymmetric field that corotates with the RZ. In addition to the fast dynamo confinement scenario first proposed by Forgács-Dajka & Petrovay (2001), we thus might also recommend exploring a slow dynamo confinement scenario. This would be similar to the model of Gough & McIntyre (1998), but with the permanent dynamo field taking the place of the primordial field. It would differ from Gough & McIntyre (1998) mainly in that no primordial field would need to be confined to the RZ.

Finally, in order to make further progress on the numerical side, future simulations need to accomplish several computationally challenging tasks. First, they need to achieve equilibrium that is not diffusively controlled. Second, they must be run in the $\sigma \lesssim 1$ regime; only then can we assess whether a dynamo confinement scenario can operate in the solar regime of little viscous torque. Finally, simulations must be run with small skin-depths $\delta_{m\omega}$ (i.e., low Ek or high ${\rm Pr_m}$). Skin-depths as small as in the Sun would not be possible, but we may at least achieve $\delta_{m\omega} < \Gamma_\odot$, which would help confirm if the permanent dynamo field could penetrate deeply enough to confine the tachocline.

APPENDIX

A. BACKGROUND STATE

Note that in this section, we discuss both the non-dimensional and dimensional versions of various quantities. To explicitly distinguish, we denote the dimensional version of a quantity with a "dim" subscript (quantities like $c_{\rm p}$ and $\tilde{\nu}$, which are always dimensional, do not require a subscript).

In terms of the dimensional background state, the perfect-gas law is

$$\overline{P}_{\rm dim} = \left[\frac{(\gamma-1)c_{\rm p}}{\gamma}\right]\overline{\rho}_{\rm dim}\overline{T}_{\rm dim}, \tag{A1}$$

hydrostatic balance is

$$\frac{d\overline{P}_{\rm dim}}{dr_{\rm dim}} = -\overline{\rho}_{\rm dim}\overline{g}_{\rm dim}, \tag{A2}$$

and the first law of thermodynamics is

$$\frac{1}{c_{\rm p}}\left(\frac{dS_{\rm dim}}{dr_{\rm dim}}\right) = \frac{d\ln\overline{T}_{\rm dim}}{dr_{\rm dim}} - \left(\frac{\gamma-1}{\gamma}\right)\frac{d\ln\overline{\rho}_{\rm dim}}{dr_{\rm dim}}. \tag{A3}$$

After non-dimensionalizing, Equations (A1)–(A3) take the form

$$\overline{P} = \overline{\rho}\overline{T}, \tag{A4}$$

$$\frac{d\overline{P}}{dr} = -{\rm Di}\left(\frac{\gamma}{\gamma-1}\right)\overline{\rho}\,\overline{g}, \tag{A5}$$

and

$$\frac{d\overline{S}}{dr} = \frac{d\ln\overline{T}}{dr} - \left(\frac{\gamma-1}{\gamma}\right)\frac{d\ln\overline{\rho}}{dr}, \tag{A6}$$

where $\overline{S} \equiv \overline{S}_{\rm dim}/c_{\rm p}$ and we recall that ${\rm Di} \equiv \tilde{g}H/(c_{\rm p}\tilde{T})$. We combine Equations (A4)–(A6) to yield

$$\frac{d\overline{T}}{dr} - \left(\frac{d\overline{S}}{dr}\right)\overline{T} = -{\rm Di}\overline{g}, \tag{A7}$$

which has the exact solution [after choosing, without loss of generality, $\overline{S}(r_0) = 0$],

$$\overline{T} = e^{\overline{S}}\left[\overline{T}(r_0) - {\rm Di}\int_{r_0}^{r}\overline{g}(x)e^{-\overline{S}(x)}dx\right]. \tag{A8}$$

We then eliminate $\overline{P}$ from Equations (A4) and (A5) to yield

$$\overline{\rho} = \overline{\rho}(r_0)\exp\left[-\left(\frac{\gamma}{\gamma-1}\right)\overline{S}\right]\overline{T}^{1/(\gamma-1)}. \tag{A9}$$

There are three equations relating $\overline{\rho}(r_0)$, $\overline{T}(r_0)$, Di, γ, β, and N_ρ: two from our choice of non-dimensionalization—$(4\pi/V_{\rm CZ})\int_{r_0}^{r_{\rm out}}\overline{\rho}(r)r^2dr = 1$ and $(4\pi/V_{\rm CZ})\int_{r_0}^{r_{\rm out}}\overline{T}(r)r^2dr = 1$, where $V_{\rm CZ} \equiv (4\pi/3)(r_{\rm out}^3 - r_0^3) = (4\pi/3)[(1-\beta^3)/(1-\beta)^3]$—and one from the definition $N_\rho \equiv \ln[\overline{\rho}(r_0)/\overline{\rho}(r_{\rm out})]$. Thus, $\overline{\rho}(r_0)$, $\overline{T}(r_0)$, and Di may be regarded as functions of γ, β, and N_ρ. For the values given in Table 1 (and our choices for $\overline{g}$ and $d\overline{S}/dr$ given below), we explicitly find $\overline{\rho}(r_0) = 2.67$, $\overline{T}(r_0) = 2.04$, and ${\rm Di} = 1.72$.

Table A1. Derived non-dimensional parameters and time-scales for our simulations, which can be obtained from Table 1 and the form of the reference state. These include the Taylor number Ta, the Rayleigh number $\mathrm{Ra_F}$, and the convective Rossby number $\mathrm{Ro_c}$. In the lower part of the table, all time-scales are non-dimensional (i.e., scaled by Ω_0^{-1}). The diffusion times (P_ν, P_η, etc.) estimate the time for different diffusive processes across different sub-domains (CZ, RZ, or full-shell) of the simulation.

Parameter	Definition	Value
$r_{\rm in}$	$(2\beta-1)/(1-\beta)$	2.15
r_0	$\beta/(1-\beta)$	3.15
$r_{\rm out}$	$1/(1-\beta)$	4.15
$N_{\rho,\rm RZ}$	$\ln[\overline{\rho}(r_{\rm in})/\overline{\rho}(r_0)]$	2.08
Di	$\tilde{g}H/c_{\rm p}\tilde{T}$	1.72
Ta	Ek^{-2}	8.80×10^5
$\mathrm{Ra_F}$	$\mathrm{Ra_F^*Pr/Ek^2}$	5.62×10^5
$\mathrm{Ro_c}$	$\sqrt{\mathrm{Ra_F^*}}/2$	0.400
$\mathrm{Ek_{RZ}}$	$\langle\overline{\nu}\rangle_{\rm RZ}\,\mathrm{Ek}$	3.47×10^{-4}
σ	$\sqrt{\mathrm{PrB}}/2$	79.6
$P_{\rm rot}$	rotation period	2π
$P_\nu = P_\kappa$	$(4/\langle\overline{\nu}\rangle_{\rm full})/\mathrm{Ek}$	779 $P_{\rm rot}$
P_η	$(4/\langle\overline{\eta}\rangle_{\rm full})\mathrm{Pr_m/Ek}$	779 to 6240 $P_{\rm rot}$
$P_{\nu,\rm CZ} = P_{\kappa,\rm CZ}$	$1/\mathrm{Ek}$	149 $P_{\rm rot}$
$P_{\eta,\rm CZ}$	$\mathrm{Pr_m/Ek}$	149 to 1190 $P_{\rm rot}$
$P_{\nu,\rm RZ} = P_{\kappa,\rm RZ}$	$1/\mathrm{Ek_{RZ}}$	459 $P_{\rm rot}$
$P_{\eta,\rm RZ}$	$\mathrm{Pr_m/Ek_{RZ}}$	459 to 3670 $P_{\rm rot}$
$P_{\rm ES}$	$P_{\kappa,\rm RZ}\mathrm{Bu}/4$	2.91×10^6 $P_{\rm rot}$

For $\overline{g}(r)\propto 1/r^2$ and the condition $(4\pi/V_{\rm CZ})\int_{r_0}^{r_{\rm out}}\overline{g}(r)r^2dr = 1$, we require

$$\overline{g}(r) = \left[\frac{1-\beta^3}{3(1-\beta)^3}\right]\frac{1}{r^2}. \tag{A10}$$

To model the transition from convective stability to instability at the base of the CZ, we choose $d\overline{S}/dr$ to be zero in the CZ, a constant positive (near-unity) value in the RZ, and continuously matched in between:

$$\frac{d\overline{S}}{dr} = \begin{cases} \Sigma & r \le r_0-\delta \\ \Sigma\left\{1-\left(1-\left(\frac{r-r_0}{\delta}\right)^2\right]^2\right\} & r_0-\delta < r < r_0 \\ 0 & r \ge r_0, \end{cases} \tag{A11}$$

where $\Sigma = 0.453$ (note that Σ is not really a free parameter, since it can always be absorbed into the fluid control parameter Bu). The choice of quartic matching ensures that the ultimate stability transition (determined by the total entropy gradient $d\overline{S}/dr + d\langle S\rangle_{\rm sph}/dr$ in the equilibrated state) is never too far from r_0. By contrast, for a tanh matching [$d\overline{S}/dr = (\Sigma/2)(1-\tanh[(r-r_0)/\delta]$); e.g., Korre & Featherstone 2021], the stability transition can occur significantly above r_0. In our cases, it could occur as high up as $r_0+5\delta$, since $d\langle S\rangle_{\rm sph}/dr$ is generally 10^4–10^5 times smaller than $d\overline{S}/dr$ and $(1/2)[1-\tanh(5)]\approx 5\times10^{-5}$.

With $d\overline{S}/dr$ and $\overline{g}$ chosen, we numerically integrate Equations (A8) and (A9) to find $\overline{\rho}$ and $\overline{T}$. This approach to defining the background state (also used by Korre & Featherstone 2021) has the main advantage that hydrostatic balance is satisfied everywhere, even in the transition region. This stands in contrast to polytropic matching (e.g., Racine et al. 2011; Guerrero et al. 2016).

Note that equation (A11) also defines the buoyancy frequency through

$$\frac{\overline{N^2}}{\overline{g}} = \frac{d\overline{S}/dr}{\langle\overline{g}d\overline{S}/dr\rangle_{\rm RZ}}, \tag{A12}$$

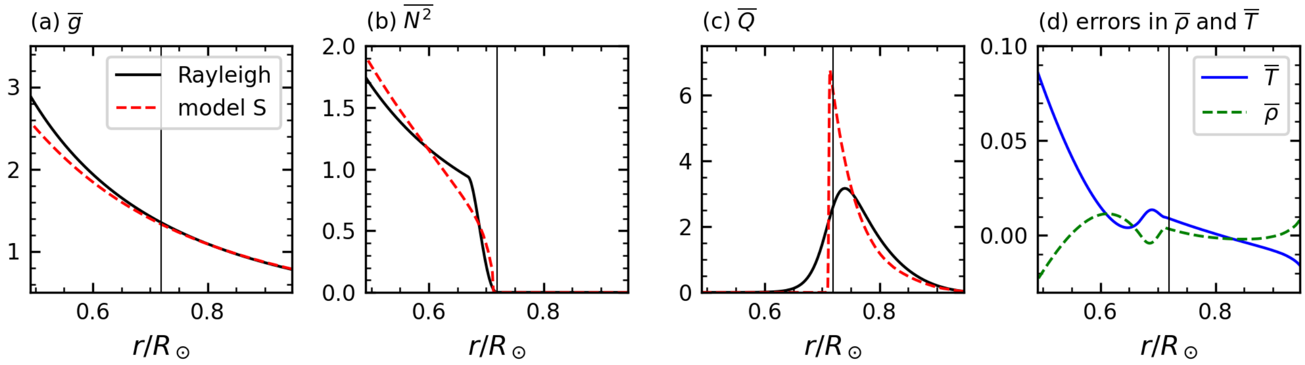

Figure A1. (a)–(c) Non-dimensional reference state (solid black curves) compared to Model S (dashed red curves). (d) Relative errors (compared to Model S) in our reference-state for $\overline{\rho}(r)$ and $\overline{T}(r)$, with the error defined as, e.g., $(\overline{\rho}-\overline{\rho}_S)/\overline{\rho}_S$. In all panels, the vertical line denotes the CZ–RZ interface $r=r_0$.

where $\langle \overline{g}d\overline{S}/dr\rangle_{\rm RZ} = 0.597$.

We choose $\overline{Q}(r)$ to occupy primarily the CZ:

$$\overline{Q} = \frac{c}{2}\left[1+\tanh\left(\frac{r-r_0}{\delta_{\rm heat}}\right)\overline{\rho}\overline{T}\right], \tag{A13}$$

where $c = 0.944$. This value of c is required because $\overline{Q} = Q_{\rm dim}H/\widetilde{F_{\rm nr}}$. The definition $(\widetilde{F_{\rm nr}})_{\rm dim} \equiv (1/Hr^2)\int_r^{r_{\rm out}} Q_{\rm dim}(x)x^2dx$ then yields $1/c = (2\pi/V_{\rm CZ})\int_{r_0}^{r_{\rm out}}(1/r^2)\int_r^{r_{\rm out}} f(x)x^2dxdr$, where $f(x) \equiv 1+\tanh[(x-r_0)/\delta_{\rm heat}]$.

Table A1 gives some additional (derivative) input parameters that can be computed from the parameters of Table 1 and the form of the reference state just described.

We compare this reference state to the standard solar Model S (Christensen-Dalsgaard et al. 1996) in Figure A1. Note that Model S profiles (denoted by an “S” subscript) are originally in dimensional form.

For the dimensional molecular diffusivities associated with Model S, we define

$$\overline{\nu}_S \equiv 1.2\times 10^{-16}\ \frac{(\overline{T}_S/{\rm K})^{5/2}}{\overline{\rho}_S/({\rm g\ cm^{-3}})}\ {\rm cm^2\ s^{-1}}, \tag{A14a}$$

$$\overline{\kappa}_S \equiv \frac{16\sigma_{\rm SB}\overline{T}_S^3}{3\overline{\chi}_S\overline{\rho}_S^2(c_{\rm p})_S}, \tag{A14b}$$

$$\overline{\eta}_S \equiv 5.2\times 10^{11}\ \frac{\ln\Lambda}{(\overline{T}_S/{\rm K})^{3/2}}\ {\rm cm^2\ s^{-1}}, \tag{A14c}$$

where $\sigma_{SB} \equiv 5.67\times 10^{-5}$ erg cm^{-2} s^{-1} K^{-4} is the Stefan-Boltzmann constant and $\overline{\chi}_S$ is the opacity from Model S. The forms of the molecular viscosity $\overline{\nu}_S$ and the radiative thermal diffusivity κ_S are given in (e.g.) Parker (1979) via Miesch (2005). The form of $\overline{\eta}_S$ is given in (e.g.) Spitzer (1962). The Coulomb logarithm $\ln\Lambda$ is tabulated by (e.g.) Stix (2002), and we approximate $\ln\Lambda \approx 2.5 + r/r_0$ (see Garaud 1999).

To non-dimensionalize Model S, we take $(R_\odot)_{\rm dim} = 6.96\times 10^{10}$ cm and set $(r_{\rm in})_{\rm dim} = 0.491(R_\odot)_{\rm dim}$, $(r_0)_{\rm dim} = 0.719(R_\odot)_{\rm dim}$, and $(r_{\rm out})_{\rm dim} = 0.947(R_\odot)_{\rm dim}$ [and thus $H = 0.228(R_\odot)_{\rm dim}$]. This choice means we compare to the bottom three density scale-heights of Model S's CZ, i.e., $\ln\{\overline{\rho}_S[(r_0)_{\rm dim}]/\overline{\rho}_S[(r_{\rm out})_{\rm dim}]\} = 3$. For a given reference-state quantity ψ, we then define $\langle\psi\rangle_{\rm CZ}$ (or $\tilde{\psi}$) as a volume average of ψ over $((r_0)_{\rm dim},(r_{\rm out})_{\rm dim})$ and $\langle\psi\rangle_{\rm RZ}$ as a volume average of ψ over $[(r_{\rm in})_{\rm dim},(r_0)_{\rm dim}]$. We then scale $\overline{\rho}_S$, $\overline{T}_S$, and $\overline{g}_S$ by $\tilde{\rho}_S$, $\tilde{T}_S$, and $\tilde{g}_S$ (respectively), $\overline{Q}_S$ by $(\widetilde{F_{\rm nr}})_S/H$, and $(\overline{N^2})_S$ by $\langle(N^2)_S\rangle_{\rm RZ}$. Then for the rest of this section, the Model S profiles denote their non-dimensional forms.

Figure A1 shows that `Rayleigh`'s non-dimensional reference state is fairly solar-like, being equivalent to the adiabatic polytrope from our prior work (e.g., Featherstone & Hindman 2016; Orvedahl et al. 2018; Matilsky et al. 2019; Hindman et al. 2020). The biggest discrepancies occur near $r=r_0$, where our reference state has relatively wide and smooth transitions in $\overline{N^2}$ and $\overline{Q}$ compared to the narrow and sharp transitions from Model S.

Note that the background diffusivities from the simulations' reference state, $\overline{\nu}$, $\overline{\kappa}$, and $\overline{\eta}$, are specified independently from the thermodynamic profiles. We choose all simulation diffusivities to increase with radius like $\overline{\rho}^{-1/2}$ (and of course they are normalized to have a volume-average over the CZ of 1). Note that this choice does not in any sense correspond to the non-dimensional Model S profiles, $\overline{\nu}_S$, $\overline{\kappa}_S$, and $\overline{\eta}_S$.

B. DIMENSIONAL SOLAR ANALOG

Here, we "re-dimensionalize" the models considered in the current paper to match the presentation of cases H and 4.00 in Paper I. A non-dimensional simulation can be re-dimensionalized by assuming dimensional values for quantities like H and Ω_0 and then computing the associated scales for the fluid variables (e.g., $[S]$ and $[\boldsymbol{u}]$) and reference-state profiles (e.g., $\tilde{\rho}$ and $\tilde{T}$), as described in Section 2. To list the input dimensional quantities in the conventional way, we define the luminosity $L \equiv \tilde{Q}V_{\rm dim}$, where $V_{\rm dim} \equiv (4\pi H^3/3)(r_{\rm out}^3 - r_{\rm in}^3)$. L is typically the control parameter that sets $\widetilde{F_{\rm nr}}$. We also define the stellar mass $M \equiv [(1-\beta^3)/3(1-\beta)^3](H^2/G)\tilde{g}$, so $\overline{g}_{\rm dim} = GM/H^2r^2$. M is typically the parameter that sets $\tilde{g}$. The full set of dimensional input parameters is then: H, Ω_0, L, M, $c_{\rm p}$, $\tilde{\rho}$, $\tilde{T}$, $\tilde{\nu}$, $\tilde{\kappa}$, $\tilde{\eta}$, and $\langle N^2\rangle_{\rm RZ}$.

Some of the input dimensional parameters are obviously redundant, so there are infinitely many ways to re-dimensionalize. The only requirement is that the chosen dimensional values be consistent with the input non-dimensional numbers. Historically, we in the solar and stellar communities have chosen stellar-like dimensional values for as many parameters as possible except for the diffusivities, which are chosen to be unrealistically high. This choice is exemplified in Table B2, which contains the scaling employed in Paper I. Most of the chosen parameters are solar-like, except for the diffusivities. The rotation rate Ω_0 is chosen to be about three times higher than the solar Carrington value.

The inherent non-uniqueness associated with dimensional simulations is one of the main reasons we report only the non-dimensional versions of the simulations in this work. For example, comparing the simulated $\boldsymbol{B}_{\rm dim}$ (measured in G) to an observed $\boldsymbol{B}$ at the solar surface (also measured in G) is fundamentally ambiguous. For, we could have re-dimensionalized using the values in Table B2, but instead chosen $\Omega_0 \rightarrow \Omega_\odot$, $L \rightarrow L_\odot/27$, $\langle N^2\rangle_{\rm RZ} \rightarrow \langle N^2\rangle_{\rm RZ}/3$, $\tilde{\nu} \rightarrow \tilde{\nu}/3$, $\tilde{\kappa} \rightarrow \tilde{\kappa}/3$, and $\tilde{\eta} \rightarrow \tilde{\eta}/3$. This would have yielded dynamically identical simulations, but with all values of $\boldsymbol{B}_{\rm dim}$ three times smaller.

C. OUTPUT NON-DIMENSIONAL NUMBERS

We define the Reynolds (Re), Rossby (Ro), and magnetic Reynolds (Re$_{\rm m}$) numbers, separately for the mean and fluctuating flows:

$$\mathrm{Re}_{\rm mean} \equiv \frac{(\langle\boldsymbol{u}\rangle_\phi)_{\rm rms}}{\mathrm{Ek}}, \qquad \mathrm{Re}_{\rm fluc} \equiv \frac{(\boldsymbol{u}')_{\rm rms}}{\mathrm{Ek}}, \tag{C15}$$

$$\mathrm{Ro}_{\rm mean} \equiv \frac{(\langle\boldsymbol{\omega}\rangle_\phi)_{\rm rms}}{2}, \qquad \mathrm{Ro}_{\rm fluc} \equiv \frac{(\boldsymbol{\omega}')_{\rm rms}}{2}, \tag{C16}$$

$$\mathrm{Re}_{\rm m,mean} \equiv \mathrm{Re}_{\rm mean}\mathrm{Pr}_{\rm m}, \qquad \mathrm{Re}_{\rm m,fluc} \equiv \mathrm{Re}_{\rm fluc}\mathrm{Pr}_{\rm m}, \tag{C17}$$

where $\boldsymbol{\omega} \equiv \nabla\times\boldsymbol{u}$ is the vorticity and the mean in the rms is taken in volume (over the CZ or RZ) and in time over the equilibrated state. Table C3 contains the values of these numbers for each simulation considered in this work.

Table B2. Paper I's re-dimensionalization of our models. Recall $[S] = \Delta S \equiv \widetilde{F_{\rm nr}} H/\tilde{\rho}\tilde{T}\tilde{\kappa}$, $[P] = \tilde{\rho}(2\Omega_0 H)^2$, $[\boldsymbol{u}] = \Omega_0 H$, $[\boldsymbol{B}] = \sqrt{\mu\tilde{\rho}}(\Omega_0 H)$, and $\mu = 4\pi$ in Gaussian units.

Quantity	Model S value	Dimensional analog value
H	1.59×10^{10} cm	1.59×10^{10} cm
Ω_0	2.70×10^{-6} rad s^{-1}	8.61×10^{-6} rad s^{-1}
$P_{\rm rot}$	26.9 days	8.45 days
L	3.40×10^{33} erg s^{-1}	$L_\odot \equiv 3.85 \times 10^{33}$ erg s^{-1}
$\widetilde{F_{\rm nr}}$	7.12×10^{10} erg cm^{-2} s^{-1}	6.79×10^{10} erg cm^{-2} s^{-1}
M	1.97×10^{33} g	$M_\odot \equiv 1.99 \times 10^{33}$ g
$\tilde{g}$	3.90×10^{4} cm sec^{-2}	3.93×10^{4} cm sec^{-2}
$\tilde{\rho}$	6.79×10^{-2} g cm^{-3}	6.75×10^{-2} g cm^{-3}
$\langle\rho\rangle_{\rm RZ}$	0.523 g cm^{-3}	0.520 g cm^{-3}
$\tilde{T}$	1.06×10^{6} K	1.03×10^{6} K
$c_{\rm p}$	3.54×10^{8} erg g^{-1} K^{-1}	3.50×10^{8} erg g^{-1} K^{-1}
$\left\langle N^2\right\rangle_{\rm RZ}$	2.03×10^{-6} (rad s^{-1})^2	1.88×10^{-6} (rad s^{-1})^2
$\tilde{\nu}$	2.21 cm^2 s^{-1}	2.31×10^{12} cm^2 s^{-1}
$\tilde{\kappa}$	3.90×10^{6} cm^2 s^{-1}	2.31×10^{12} cm^2 s^{-1}
$\tilde{\eta}$	3.09×10^{3} cm^2 s^{-1}	(0.289–2.31)$\times 10^{12}$ cm^2 s^{-1}
$\langle\nu\rangle_{\rm RZ}$	4.15 cm^2 s^{-1}	7.51×10^{11} cm^2 s^{-1}
$\langle\kappa\rangle_{\rm RZ}$	9.70×10^{6} cm^2 s^{-1}	7.51×10^{11} cm^2 s^{-1}
$\langle\eta\rangle_{\rm RZ}$	3.61×10^{2} cm^2 s^{-1}	(0.939–7.51)$\times 10^{11}$ cm^2 s^{-1}
$(P_{\nu,{\rm RZ}})_{\rm dim}$	1.92×10^{12} years	10.6 years
$(P_{\eta,{\rm RZ}})_{\rm dim}$	2.21×10^{10} years	(10.6–84.9) years
$(P_{\rm ES})_{\rm dim}$	5.72×10^{10} years	6.73×10^{4} years
$[S]$	4.04×10^{9} erg g^{-1} K^{-1}	6.69×10^{3} erg g^{-1} K^{-1}
$[P]$	1.24×10^{8} erg cm^{-3}	2.01×10^{10} erg cm^{-3}
$[\boldsymbol{u}]$	4.28×10^{4} m s^{-1}	1.40×10^{3} m s^{-1}
$[\boldsymbol{B}]$	3.95×10^{4} G	1.26×10^{5} G

Table C3. Output non-dimensional numbers, defined in Equations (C15)–(C17), for all simulations. The number values in the CZ and RZ are given separately.

Case	H	1.00	1.05	1.06	1.08	1.33	1.67	2.00	3.00	4.00	6.00	8.00
regime	-	W	W	W	M	M	M	M	S	S	S	S
CZ non-dimensional numbers												
$\mathrm{Re}_{\rm mean}$	173.9	174.1	173.8	173.1	85.56	71.06	66.36	65.93	45.51	40.63	34.69	30.28
$\mathrm{Re}_{\rm fluc}$	68.74	68.76	68.47	68.58	58.05	57.81	57.65	57.57	57.25	56.77	56.33	55.95
$\mathrm{Ro}_{\rm mean}$	0.144	0.145	0.144	0.144	0.097	0.085	0.081	0.079	0.063	0.057	0.050	0.045
$\mathrm{Ro}_{\rm fluc}$	0.438	0.438	0.437	0.438	0.436	0.435	0.433	0.432	0.428	0.423	0.423	0.423
$\mathrm{Re}_{\rm m,mean}$	-	174.1	183.2	184.3	92.09	94.75	110.6	131.9	136.5	162.5	208.2	242.2
$\mathrm{Re}_{\rm m,fluc}$	-	68.76	72.15	73.03	62.49	77.08	96.09	115.1	171.8	227.1	338.0	447.6
RZ non-dimensional numbers												
$\mathrm{Re}_{\rm mean}$	219.1	219.8	219.1	216.9	61.86	57.08	51.85	53.40	13.42	10.84	10.06	8.757
$\mathrm{Re}_{\rm fluc}$	45.19	45.15	44.48	44.86	16.15	13.05	12.26	11.97	10.43	10.21	9.850	9.534
$\mathrm{Ro}_{\rm mean}$	0.070	0.070	0.070	0.069	0.025	0.021	0.020	0.020	9.3e-3	8.0e-3	7.1e-3	6.4e-3
$\mathrm{Ro}_{\rm fluc}$	0.076	0.076	0.075	0.075	0.043	0.040	0.039	0.039	0.036	0.035	0.035	0.034
$\mathrm{Re}_{\rm m,mean}$	-	219.8	230.9	231.0	66.58	76.11	86.42	106.8	40.27	43.35	60.37	70.06
$\mathrm{Re}_{\rm m,fluc}$	-	45.15	46.88	47.78	17.39	17.40	20.43	23.95	31.30	40.83	59.10	76.28

ACKNOWLEDGMENTS

We thank the following (undoubtedly incomplete) list of individuals for helpful discussions of the solar tachocline: Pascale Garaud, Mark Miesch, Lydia Korre, Nicholas Featherstone, Gustavo Guerrero, Connor Bice, Sacha Brun, Antoine Strugarek, Catherine Blume, Matthew Browning, Steven Tobias, David Hughes, and Jørgen Christensen-Dalsgaard. This work was partly done in collaboration with the COFFIES DRIVE Science Center (NASA grant 80NSSC22M0162). L.I.M. and N.H.B. thank the Isaac Newton Institute for Mathematical Sciences (Cambridge, UK) for support and hospitality during the 2022 Programme "Frontiers in Dynamo Theory: from the Earth to the Sun and Stars", where part of the work on this paper was undertaken. L.I.M. was primarily supported during this work by a National Science Foundation Astronomy & Astrophysics Postdoctoral Fellowship under award AST-2202253, as well as a Future Investigators in NASA Earth and Space Sciences Technology (FINESST) award 80NSSC19K1428. The computations integral to this work were supported by NASA grant 80NSSC18K1127. This research was further supported by NASA grants 80NSSC18K1125, 80NSSC19K0267, and 80NSSC20K0193. Computational resources were provided by the NASA High-End Computing (HEC) Program through the NASA Advanced Supercomputing (NAS) Division at Ames Research Center. `Rayleigh` is hosted and receives support from the Computational Infrastructure for Geodynamics (CIG), which is supported by the National Science Foundation awards NSF-0949446, NSF-1550901, and NSF-2149126. The input files, final checkpoints, and some data-analysis products (averaged data and basic plots) for all simulations are publicly accessible via Zenodo (Matilsky et al. 2023).

REFERENCES

Acevedo-Arreguin, L. A., Garaud, P., & Wood, T. S. 2013, MNRAS, 434, 720, doi: 10.1093/mnras/stt1065

Augustson, K., Brun, A. S., Miesch, M., & Toomre, J. 2015, ApJ, 809, 149, doi: 10.1088/0004-637x/809/2/149

Aurnou, J. M., & Aubert, J. 2011, PEPI, 187, 353, doi: 10.1016/j.pepi.2011.05.011

Bai, T. 2003, ApJ, 585, 1114, doi: 10.1086/346152

Barnabé, R., Strugarek, A., Charbonneau, P., Brun, A. S., & Zahn, J.-P. 2017, A&A, 601, A47, doi: 10.1051/0004-6361/201630178

Basu, S., & Antia, H. M. 2003, ApJ, 585, 553, doi: 10.1086/346020

Berdyugina, S. V., & Usoskin, I. G. 2003, A&A, 405, 1121, doi: 10.1051/0004-6361:20030748

Bice, C. P., & Toomre, J. 2020, ApJ, 893, 107, doi: 10.3847/1538-4357/ab8190

—. 2023, ApJ, 951, 79, doi: 10.3847/1538-4357/acd2db

Bigazzi, A., & Ruzmaikin, A. 2004, The Astrophysical Journal, 604, 944, doi: 10.1086/381932

Bogart, R. S. 1982, SoPh, 76, 155, doi: 10.1007/bf00214137

Braun, D. C., Birch, A. C., & Fan, Y. 2021, ApJ, 911, 54, doi: 10.3847/1538-4357/abe7e4

Brown, B. P., Browning, M. K., Brun, A. S., Miesch, M. S., & Toomre, J. 2010, ApJ, 711, 424, doi: 10.1088/0004-637x/711/1/424

Brun, A. S., & Browning, M. K. 2017, LRSP, 14, 4, doi: 10.1007/s41116-017-0007-8

Charbonneau, P., Christensen-Dalsgaard, J., Henning, R., et al. 1999, ApJ, 527, 445, doi: 10.1086/308050

Chen, R., & Zhao, J. 2017, ApJ, 849, 144, doi: 10.3847/1538-4357/aa8eec

Christensen, U. R., & Aubert, J. 2006, Geophysical Journal International, 166, 97, doi: 10.1111/j.1365-246x.2006.03009.x

Christensen-Dalsgaard, J., Däppen, W., Ajukov, S. V., et al. 1996, Sci., 272, 1286, doi: 10.1126/science.272.5266.1286

Clark, A. 1973, JFM, 60, 561, doi: 10.1017/s0022112073000340

Clune, T., Elliott, J., Miesch, M., Toomre, J., & Glatzmaier, G. 1999, Parallel Comp., 25, 361, doi: 10.1016/s0167-8191(99)00009-5

Cope, L., Garaud, P., & Caulfield, C. P. 2020, JFM, 903, A1, doi: 10.1017/jfm.2020.600

D'Silva, S., & Choudhuri, A. R. 1993, A&A, 272, 621

Elliott, J. R. 1997, A&A, 327, 1222

Featherstone, N. A., Edelmann, P. V. F., Gassmoeller, R., et al. 2021, Rayleigh 1.0.1, doi: 10.5281/zenodo.1158289

Featherstone, N. A., & Hindman, B. W. 2016, ApJ, 818, 32, doi: 10.3847/0004-637x/818/1/32

Ferraro, V. C. A. 1937, MNRAS, 97, 458, doi: 10.1093/mnras/97.6.458

Forgács-Dajka, E. 2004, A&A, 413, 1143, doi: 10.1051/0004-6361:20031569

Forgács-Dajka, E., & Petrovay, K. 2001, SoPh, 203, 195, doi: 10.1023/a:1013389631585

—. 2002, A&A, 389, 629, doi: 10.1051/0004-6361:20020586

Garaud, P. 1999, MNRAS, 304, 583, doi: 10.1046/j.1365-8711.1999.02338.x

—. 2020, ApJ, 901, 146, doi: 10.3847/1538-4357/ab9c99

Garaud, P., & Acevedo-Arreguin, L. A. 2009, ApJ, 704, 1, doi: 10.1088/0004-637x/704/1/1

Garaud, P., & Brummell, N. H. 2008, ApJ, 674, 498, doi: 10.1086/524837

Gilman, P. A. 2000, SoPh, 192, 27, doi: 10.1023/a:1005280502744

Gilman, P. A., & Glatzmaier, G. A. 1981, ApJS, 45, 335, doi: 10.1086/190714

Glatzmaier, G. A. 1984, J. Comp. Phys., 55, 461, doi: 10.1016/0021-9991(84)90033-0

Gough, D. O. 1969, J. Atmos. Soc., 26, 448, doi: 10.1175/1520-0469(1969)026⟨0448:taaftc⟩2.0.co;2

Gough, D. O., & McIntyre, M. E. 1998, Nat., 394, 755, doi: 10.1038/29472

Greer, B. J., Hindman, B. W., Featherstone, N. A., & Toomre, J. 2015, ApJ, 803, L17, doi: 10.1088/2041-8205/803/2/l17

Greer, B. J., Hindman, B. W., & Toomre, J. 2016, ApJ, 824, 4, doi: 10.3847/0004-637x/824/1/4

Guerrero, G., Smolarkiewicz, P. K., de Gouveia Dal Pino, E. M., Kosovichev, A. G., & Mansour, N. N. 2016, ApJ, 819, 104, doi: 10.3847/0004-637x/819/2/104

Guerrero, G., Zaire, B., Smolarkiewicz, P. K., et al. 2019, ApJ, 880, 6, doi: 10.3847/1538-4357/ab224a

Hathaway, D. H. 2015, LRSP, 7, 1, doi: 10.12942/lrsp-2010-1

Haynes, P. H., McIntyre, M. E., Shepherd, T. G., Marks, C. J., & Shine, K. P. 1991, J. Atm. Sci., 48, 651, doi: 10.1175/1520-0469(1991)048⟨0651:otcoed⟩2.0.co;2

Henney, C. J., & Harvey, J. W. 2002, SoPh, 207, 199, doi: 10.1023/a:1016265629455

Hindman, B. W., Featherstone, N. A., & Julien, K. 2020, ApJ, 898, 120, doi: 10.3847/1538-4357/ab9ec2

Hotta, H., Rempel, M., & Yokoyama, T. 2015, ApJ, 798, 51, doi: 10.1088/0004-637x/798/1/51

Howe, R. 2009, LRSP, 6, 1, doi: 10.12942/lrsp-2009-1

—. 2023, Mean solar rotation profile from GONG splittings 1995-2009, Zenodo, doi: 10.5281/ZENODO.8171572

Howe, R., Christensen-Dalsgaard, J., Hill, F., et al. 2005, ApJ, 634, 1405, doi: 10.1086/497107

Ivanov, E. 2007, Adv. Space Res., 40, 959, doi: 10.1016/j.asr.2007.02.093

Ivanova, T. S., & Ruzmaikin, A. A. 1985, Astron. Nach., 306, 177, doi: 10.1002/asna.2113060402

Korre, L., & Featherstone, N. A. 2021, ApJ, 923, 52, doi: 10.3847/1538-4357/ac2dea

Kosovichev, A. G. 1996, ApJ, 469, L61, doi: 10.1086/310253

Li, J. 2018, ApJ, 867, 89, doi: 10.3847/1538-4357/aae31a

Matilsky, L. I. 2023, MNRAS, doi: 10.48550/ARXIV.2307.09422

Matilsky, L. I., Brummell, N. H., Hindman, B. W., & Toomre, J. 2023, Simulation data-set for ApJ Article: Confinement of the Solar Tachocline by a Non-Axisymmetric Dynamo, Zenodo, doi: 10.5281/zenodo.10140423

Matilsky, L. I., Hindman, B. W., Featherstone, N. A., Blume, C. C., & Toomre, J. 2022, ApJL, 940, L50, doi: 10.3847/2041-8213/ac93ef

Matilsky, L. I., Hindman, B. W., & Toomre, J. 2019, ApJ, 871, 217, doi: 10.3847/1538-4357/aaf647

—. 2020, ApJ, 898, 111, doi: 10.3847/1538-4357/ab9ca0

Matilsky, L. I., & Toomre, J. 2020a, ApJ, 892, 106, doi: 10.3847/1538-4357/ab791c

—. 2020b, in Astrophysics and Space Science Proceedings (Springer International Publishing), 197–199, doi: 10.1007/978-3-030-55336-4_27

Matilsky, L. I., & Toomre, J. 2021, in 20.5th Cambridge Workshop on Cool Stars, Stellar Systems, and the Sun, ed. S. J. Wolk (Zenodo), doi: 10.5281/ZENODO.4750777

Matsui, H., Heien, E., Aubert, J., et al. 2016, Geochem., Geophys., Geosys., 17, 1586, doi: 10.1002/2015gc006159

Maunder, E. 1905, MNRAS, 65, 538

McIntyre, M. 1994, in The Solar Engine and its Influence on Terrestrial Atmosphere and Climate, ed. E. Nesme-Ribes, 293

Miesch, M. S. 2005, LRSP, 2, 1, doi: 10.12942/lrsp-2005-1

Miesch, M. S., & Hindman, B. W. 2011, ApJ, 743, 79, doi: 10.1088/0004-637x/743/1/79

Moffatt, H., & Dormy, E. 2019, Self-Exciting Fluid Dynamos (Cambridge: Cambridge University Press)

Mordvinov, A. V., & Kitchatinov, L. L. 2004, Astron. Rep., 48, 254, doi: 10.1134/1.1687019

Moss, D., Piskunov, N., & Sokoloff, D. 2002, A&A, 396, 885, doi: 10.1051/0004-6361:20021370

Nagashima, K., Birch, A. C., Schou, J., Hindman, B. W., & Gizon, L. 2020, A&A, 633, A109, doi: 10.1051/0004-6361/201936662

Nelson, N. J., Brown, B. P., Brun, A. S., Miesch, M. S., & Toomre, J. 2013a, SoPh, 289, 441, doi: 10.1007/s11207-012-0221-4

Ogura, Y., & Phillips, N. A. 1962, J. Atm. Sci., 19, 173, doi: 10.1175/1520-0469(1962)019⟨0173:saodas⟩2.0.co;2

Olemskoy, S. V., & Kitchatinov, L. L. 2009, Geomagnetism and Aeronomy, 49, 866, doi: 10.1134/s001679320907007x

Orvedahl, R. J., Calkins, M. A., Featherstone, N. A., & Hindman, B. W. 2018, ApJ, 856, 13, doi: 10.3847/1538-4357/aaaeb5

Parker, E. N. 1979, Astrophysics and Space Science, 62, 135, doi: 10.1007/bf00643907

Passos, D., & Charbonneau, P. 2014, A&A, 568, A113, doi: 10.1051/0004-6361/201423700

Racine, É., Charbonneau, P., Ghizaru, M., Bouchat, A., & Smolarkiewicz, P. K. 2011, ApJ, 735, 46, doi: 10.1088/0004-637x/735/1/46

Spiegel, E. A., & Zahn, J.-P. 1992, A&A, 265, 106

Spitzer, L. 1962, Physics of Fully Ionized Gases, 2nd Ed. (New York: Interscience Publishers)

Starr, V. P. 1968, Physics of Negative-Viscosity Phenomena (New York: McGraw Hill)

Stenflo, J. O., & Kosovichev, A. G. 2012, ApJ, 745, 129, doi: 10.1088/0004-637x/745/2/129

Stix, M. 1971, A&A, 13, 203

Stix, M. 2002, The Sun (Springer Berlin Heidelberg), doi: 10.1007/978-3-642-56042-2

Svalgaard, L., & Wilcox, J. M. 1975, SoPh, 41, 461, doi: 10.1007/bf00154083

Tobias, S. M., Diamond, P. H., & Hughes, D. W. 2007, ApJ, 667, L113, doi: 10.1086/521978

Usoskin, I. G. 2013, LRSP, 10, doi: 10.12942/lrsp-2013-1

Wilson, P. R., Burtonclay, D., & Li, Y. 1996, ApJ, 457, 440, doi: 10.1086/176744

Wood, T. S., & Brummell, N. H. 2012, ApJ, 755, 99, doi: 10.1088/0004-637x/755/2/99

—. 2018, ApJ, 853, 97, doi: 10.3847/1538-4357/aaa6d5

Yadav, R. K., Christensen, U. R., Morin, J., et al. 2015, ApJ, 813, L31, doi: 10.1088/2041-8205/813/2/l31

Zhao, J., Nagashima, K., Bogart, R. S., Kosovichev, A. G., & Duvall, T. L. 2012, ApJ, 749, L5, doi: 10.1088/2041-8205/749/1/l5